

Imperial College London

DEPARTMENT OF PHYSICS
BLACKETT LABORATORY



MASTER THESIS:

Interaction of Interplanetary Coronal Mass Ejections in the Inner Heliosphere

3D magnetohydrodynamic parametric study using linear
force-free spheromaks

Author:
Gordon J. Köhn

Supervisor:
Dr. Ravindra Desai

A report submitted for the degree of

MSc Physics

September 10, 2021

Abstract

Coronal Mass Ejections (CMEs) are the largest type of eruptions on the Sun and are one of the main drivers of space weather. Their interaction with the magnetosphere can cause hazardous conditions to our infrastructure with severe consequences. Understanding their propagation in the inner heliosphere to Earth is extremely important for our electrified society.

This study implements a novel model, called the Linear Force-Free Spheromak (LFFS), for simulating coronal mass ejections in a representative heliosphere. This new model allows to quantify the effect of the internal magnetic structure of CMEs and their interaction, and hence significantly enhances the simulation capability of their impact on Earth's magnetosphere.

The aim of this parametric study is, to explore the impact of CME-CME interactions of different magnetic field orientations and time between successive ejections on the space weather at Earth with this new model. The impact of the magnetic field orientation for single CMEs and well as CME-CME interactions is quantified. Further, a distinct relationship between waiting time between successive CME and the dynamic and magnetic space weather conditions at Earth is established.

These findings provide a better understanding for how CMEs can enhance each other to create a perfect storm of 'Carrington' scale.

Keywords: coronal mass ejections (CMEs), heliosphere, space weather, magnetohydrodynamics (MHD), methods: highly computational, numerical

Contents

Abstract	i
1 Introduction	1
1.1 Background	2
1.1.1 Structure of CMEs and Occurrence	2
1.1.2 Impact on Magnetosphere & Infrastructure	3
2 Simulation Development	5
2.1 Governing Equations	5
2.2 Numerical Setup	6
2.3 Solar Wind & Parker Spiral	6
2.4 CME Models	10
2.4.1 Cone Model	10
2.4.2 Earlier Flux-Rope Models	10
2.4.3 Linear Force-Free Spheromak CME Model	11
2.5 Verification of Stability of Spheromak	14
2.6 Injection/Insertion of the Spheromak in the Heliosphere	15
2.6.1 Difficulties with Injecting	15
2.6.2 Inserting the Spheromak and its Implications	16
2.7 Initialization of Internal Magnetic Field	17
2.8 Virtual Spacecraft	18
3 Parametric Study	19
3.1 Input Parameters of Spheromak	19
3.2 Quantifying Geoeffectivness	20
3.3 ICME Signatures & Verification of Model	22
3.4 Stage 1: Tilt Angle	27
3.5 Stage 2: Waiting Time	31
3.6 Stage 3: Handedness	39
4 Discussion & Conclusion	45
Acknowledgements & Declaration of Work	47
Appendices	48
Appendix A Spherical Bessel Function of Order One	48
Appendix B From ϕ_t to Spheromak Parameters	49
Appendix C Coordinate Transformations and Vector Translations	50
Appendix D Simulation Code	52
Appendix E Waiting Time Simulation Runs	53
Appendix F Handedness Simulation Runs	57

1 Introduction

Coronal mass ejections (CMEs) are the largest type of eruption seen on our Sun. They are expulsions of mass and magnetic field releasing copious amounts of energy from active regions on the solar corona into the solar wind over the course of several hours. The event produces a large-scale reconfiguration of the coronal magnetic field and plasma of a mass of $10^{11} - 10^{13}$ g is expelled. Once a CME leaves the proximity of Sun, then also referred to as a *interplanetary CME* (ICME), it can propagate at velocities significantly larger than the ambient solar wind and will thus be decelerated due to drag forces. [1] The strongest CMEs still arriving at Earth may cause a significant disturbance to the magnetosphere of Earth, called a *geomagnetic storm*. Severe geomagnetic storms pose a threat to spacecraft and ground-based infrastructure.

Most of these storms are created by the passage of a single ICME (about 60%), yet a significant fraction (about 27%) have been found to be caused by the interaction of individual ICMEs with other transients, such as other CMEs or stream interaction regions. [2] [3] Several studies already established that CME-CME interactions [4] and a preconditioning of the solar wind (clearing of the path for a second ICME)(e.g. [5] and [6]) are the likely to be causal mechanisms for an increase in geoeffectivness, i.e. the severity of the impact on Earth. Yet quantification of this amplification has rarely been investigated (e.g. [7] and [8]).

For the past decade, in space weather operations, CMEs have mainly been modeled using the *cone model*, where the ejecta are treated as a hydrodynamic pulse expanding by self-similar geometry. [9] [10] [11] Such models do neglect the intrinsic magnetic field structure of the CME and model them merely as velocity, density and pressure enhancement. As such, these models fail to accurately model the impact of CMEs on the magnetic space weather conditions at Earth, thus their predictive capabilities are limited. The most recent CME models attempt to model CMEs with an intrinsic magnetic field structure as a spheromak or toroidal like flux rope structure. This brings significant advancements to modeling the impact on the magnetic space weather conditions at Earth. [12] [13] The parameters of the model for a single CME situation have been explored by multiple papers, as well as it has been shown that this model is suitable to model CME-CME interactions. [14]

This study uses this novel ICME model to simulate CME-CME interactions based on idealized parameters estimated from satellite observations in a representative heliosphere. The goal of this study is to quantify the amplification of geoeffectivness due to CME-CME interactions dependent on waiting time between successive CMEs and magnetic orientation of the internal magnetic field structure.

This report is structured as follows: The remainder of Section 1.1 gives a descriptive background about the CMEs and how the magnetosphere and infrastructure are affected by them. Section 2 provides a detailed description of the implementation of the *Linear Force-Free Spheromak model* employed to model CMEs as well as setting up a representative heliosphere using the PLUTO code magnetohydrodynamics environment. Section 3 contains the design and analysis of the parametric study simulations, followed by a discussion of the results and future prospects in Section 4.

1.1 Background

The sun is virtually the only source of energy and variability in our solar system. The energy from the Sun is provided mainly in the form of electromagnetic radiation over a very wide frequency range. However energy is also emitted in the form of particles forming the *solar wind*. The solar wind is a continuous outstreaming of plasma from the solar atmosphere which becomes supersonic above a few solar radii. It is the source of space plasmas throughout the solar system. Transient outbursts of the sun - *coronal mass ejections* - and *solar flares* - provide short term variations to the state of the solar wind. The state of the solar wind in the heliosphere is called *space weather*, and is constantly monitored for its potential impact on our infrastructure.

1.1.1 Structure of CMEs and Occurrence

CMEs are more common at solar maximum and in the declining phase of the solar cycle. They are observed using a coronagraph, an instrument designed to observe the faint corona, by artificially screening the solar disk. Thompson scattering of solar photons in the line of sight allows to see enhanced free electron densities and hence the free electron mass structure of a CME in the corona. [15]

The great amounts of observational data show that CMEs occur in two types. Narrow CMEs and normal CMEs. Narrow CMEs show jet like motions, probably along a magnetic field line. Normal CMEs show a typical morphology of a three part structure: a bright leading loop, a dark cavity surrounded by the loop, and a bright core embedded in the cavity, see Figure 1. [16] Most models focus on normal CMEs due to their greater potential impact.

Whereas the mass structure and velocity of CMEs are directly accessible from observations, little direct observational knowledge of the coronal magnetic field exists, as due to the corona's high temperature of 2×10^6 K it is difficult to determine it by spectroscopic means. [17]

Therefore, much of what is known about the magnetic structure of the corona and CMEs is based on inference. Due to the high temperatures in the corona the plasma is practically a perfect conductor, so the magnetic field is frozen into the plasma. The motion of the coronal plasma is dominated by the magnetic field, i.e. $\beta \ll 1$, and hence the apparent channelings of moving plasma are roughly interpreted to be delineating bundles of magnetic lines.

These observations about the structure of CMEs build the foundation for all the following models in Section 2.4.

The frequency of occurrence of the most extreme of all ICMEs are though to occur within a power law distribution. [18] The most famous of all is the Carrington Event, which hit Earth with velocities of >2000 kms⁻¹ and propagated from Sun to Earth within just 17.6 hours [18] and induced the largest geomagnetic storm on record. [19] Such an event would nowadays cause catastrophic consequences on our electrified society, as large scale blackouts of power grids. On 23 July 2012, another event was recorded to have missed Earth of a magnitude comparable to the 1859 Carrington event. [20]

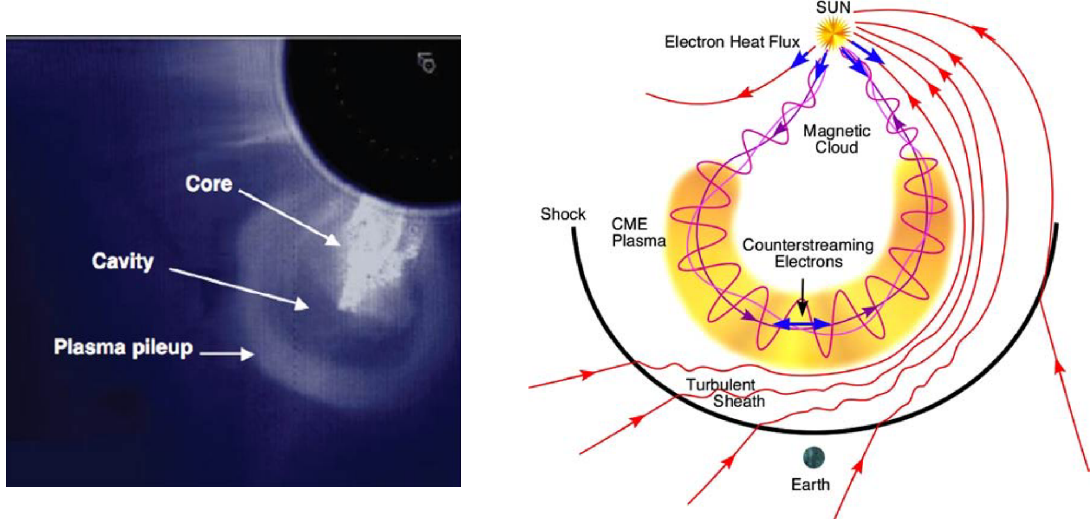


Figure 1: *Left:* Image of a coronal mass ejection showing the typical three part structure consisting of a bright core region, a cavity and plasma pileup or bright leading loop (Image from [21]);

Right: Schematic of the three-dimensional structure of an interplanetary coronal mass ejection having propagated close to Earth and its upstream shock, related magnetic field, plasma, and beams of suprathermal (100 eV) electrons. (Figure from [22])

1.1.2 Impact on Magnetosphere & Infrastructure

For context and to understand the design of parametric study a brief description of how Earth's magnetosphere and potentially space- as well as ground-based infrastructure are impacted by coronal mass ejections is given here.

When a coronal mass ejection hits Earth's magnetosphere it causes a major disturbance to it, which is called a *geomagnetic storm*. In essence, it is a very efficient energy transfer from the solar wind into the space environment surrounding Earth. More specifically these storms are caused by variations in the solar wind, which have an impact on currents, plasmas and fields in Earth's magnetosphere. The most severe geomagnetic storms are caused by solar wind conditions, which sustain high-speed and most importantly a southward directed solar wind magnetic field at the day-side of the magnetosphere for several hours. A southward directed magnetic field of the solar wind is opposite to the direction of the magnetosphere and may lead to a reconnection of magnetic field lines mediating the effective transfer of magnetic energy.

Strong geomagnetic storm result in intense currents in the magnetosphere which can damage spacecrafts. A particular current westward around Earth can even produce magnetic disturbances on the ground leading to geomagnetically induced currents in ground-based infrastructure. A measure of this current, called the Disturbance storm time (Dst) index, has historically been used to characterise the size of geomagnetic storms and shall be introduced later. These geomagnetically induced currents appear as quasi-DC currents on top of the AC frequency, and can cause half-cycle saturation of transformers, potentially damaging or destroying them. This can also lead to voltage instabilities which in turn can cause a cascading failure of the power

grid. The most famous example of this is the 1989 failure of the Hydro-Quebec power system resulting in a loss of electricity to six million people for up to 9 h.

2 Simulation Development

2.1 Governing Equations

The PLUTO code used in this project is an open source multi-physics, multi-algorithm modular environment designed for simulating astrophysical plasmas. It is designed to solve a general system of conservation laws written as

$$\frac{\partial \mathbf{U}}{\partial t} = -\nabla \cdot \mathbf{T}(\mathbf{U}) + \mathbf{S}(\mathbf{U}), \quad (1)$$

where \mathbf{U} is a state vector of conserved quantities, \mathbf{T} is a rank 2 tensor of \mathbf{U} and \mathbf{S} , where \mathbf{S} again defines the source terms. PLUTO provides the flexibility of implementing different physical equations as this general integration is not dependent on \mathbf{U} , \mathbf{T} and \mathbf{S} . It can solve non-relativistic, relativistic hydrodynamic (HD) and magnetohydrodynamic (MHD) systems in cartesian, cylindrical and spherical coordinate systems.

The PLUTO code has been validated against several benchmarks and test-problems typically adopted for alike numerical schemes. It has been extensively applied for the study of astrophysical plasmas. (e.g. [23] [24] [25] [26])

A comprehensive account of the code's capabilities is presented by *Mignone et al. (2007)* [27], yet for completeness is the system of equations, solved in this project, described below. The MHD conservation equations include the conservation of mass equation

$$\frac{\partial \rho}{\partial t} + \nabla \cdot \rho \mathbf{v} = 0, \quad (2)$$

conservation of momentum equation

$$\frac{\partial \mathbf{m}}{\partial t} + \nabla \cdot [\mathbf{m}\mathbf{v} - \mathbf{B}\mathbf{B} + \mathbf{I}(p + \mathbf{B}^2)]^T = -\rho \nabla \Phi + \rho \mathbf{g}, \quad (3)$$

Faraday's Law

$$\frac{\partial \mathbf{B}}{\partial t} + \nabla \times (\mathbf{v} \times \mathbf{B}) = 0, \quad (4)$$

conservation of energy equation

$$\frac{\partial(E_t + \rho\Phi)}{\partial t} + \nabla \cdot \left[\left(\frac{\rho\mathbf{v}^2}{2} + \rho e + p + p\Phi \right) \mathbf{v} + (\mathbf{v} \times \mathbf{B}) \times \mathbf{B} \right] = \mathbf{m} \cdot \mathbf{g}, \quad (5)$$

where \mathbf{v} is the gas velocity in the inertial reference frame, ρ is the gas mass density, p is the thermal pressure, $m = \rho\mathbf{v}$ is the momentum density and \mathbf{I} is the unit tensor. In the above equations Φ and \mathbf{g} represent the potential and vector of the body force, which has been neglected in this study. Furthermore, the total number density n is defined by $\rho = \mu H$, with μ being the mean molecular mass in units of hydrogen atoms. \mathbf{B} is the magnetic field and the total energy density E_t is expressed as

$$E_t = \rho e + \frac{\mathbf{m}^2}{2\rho} + \frac{\mathbf{B}^2}{2}. \quad (6)$$

The electric field \mathbf{E} in Equations 4 and 5 is given by the generalized Ohm's law, where the resistive and Hall terms are neglected for this study. Thereby, the system is described in the ideal MHD regime. As the closure relation to the system the equation of state $\rho e = \rho e(p, \rho)$, representing an ideal gas, has been chosen.

2.2 Numerical Setup

The system of equations presented in Section 2.1 is evolved over time using volume averages determined by a piece-wise interpolation inside each grid cell. This generic implementation allows to apply many different solvers. This study is facilitated by the *Harten-Lax-van-Leer* disContinuities (hllc) approximate Riemann solver for ideal magnetohydrodynamics presented by *Fuksman & Mignone (2019)* [28].

The model presented in this report consists of a three-dimensional ideal MHD simulation that self-consistently models the background solar wind in the inner heliosphere as well as the insertion and evolution of multiple CMEs. The ideal MHD equations are solved in a frame corresponding to the *Heliocentric Earth EQuatorial* (HEEQ) system. In this system the z-axis is parallel to the Sun's rotation axis with the positive to the North and its x-axis towards the intersection of the solar equator and the solar central meridian as seen from the Earth. The actual computational coordinate system used is spherical and defined with respect to the HEEQ system axis as commonly used in physics in line with the ISO 80000-2:2019 convention. The physical computational domain extends from 0.1 AU($\approx 21.50 R_s$) to 1.1 AU ($\approx 215.03 R_s$) and spans in latitude $\theta[30^\circ, 150^\circ]$ and longitude $\phi[-60^\circ, 60^\circ]$. This reduction of the simulation volume to a solid angle volume with opening angle of 60° allows to capture all dynamics of the CMEs studies conducted here, whilst reducing the computational requirements. The static computational grid has 60 cells in angular directions and 273 in radial, leading to a typical resolution of $0.788 R_s$ radially and 2° angular. (e.g. [12]) An error convergence analysis was conducted up to a resolution 3.3x this one, to establish that the solution achieved convergence at this finite grid resolution.

The inner radial boundary of the simulation domain implements an inflow boundary by updating ghost cells with representative solar wind values. The ϕ -boundaries, defined by the coordinate range above, are implementing periodic boundary conditions, whereas all other boundaries of r, θ are implemented by *Von-Neumann* boundary conditions for continuous outflow.

2.3 Solar Wind & Parker Spiral

To simulate the dynamics of the propagation of coronal mass ejections accurately, the environment has to represent realistic conditions of the heliosphere. The conditions in the heliosphere are defined by the solar wind, if solar eruptions as CMEs and flares are put aside. The solar wind is a continuous stream of highly energetic ionized particles being expelled from the Sun's upper corona at speeds between 250-750 km/s. The solar wind has two fundamental states related to the region of origin on the Sun: a slow and a fast, determined by their velocity being around 300 km/s or 700km/s. The slow solar wind appears to originate from a region around the Sun's equatorial belt that is known as the 'streamer belt'. The particles have energies of 0.5 to 10 keV. The particles mostly consist of electrons and protons, but also some heavier elements C, N, O, Ne, Mg, Si, S, and Fe. To reflect the fact that some heavier ions are present in the hydrogen plasma a mean molecular mass of $\mu = 0.6$ has been chosen in this project.

At the radial inner boundary the solar wind was imposed through ghost cells setting typical values of a slow solar wind. The slow solar wind was selected as the streamer belt is located around the Sun's equator, where later CMEs are to be placed in this

v_r [km s $^{-1}$]	ρ [m $_p$ cm $^{-3}$]	T [K]	B_r [nT]	B_θ [nT]	B_ϕ [nT]
300	666.6	$1.5 \cdot 10^6$	540	0	$-72.738 \cdot \sin \theta$

Table 1: Parameters imposed at inner radial boundary at 0.1 AU from the Sun to represent the slow solar wind. B_ϕ is subject to a sinusoidal variation in the HEEQ reference frame.

study.

The ghost cells of the inner boundary were set to representative conditions in velocity, density, temperature, pressure and magnetic field. The evolution of the physical variables was checked against the desired real physical conditions at Earth's position. At Earth the slow solar wind should result in $(v_r)_E = 350$ to 500 km/s, $\rho_E = 5$ m $_p$ /cm 3 and a southward magnetic field of -5 to 5 nT.

The velocity at the inner radial boundary was chosen to be $(v_r)_0 = 300$ km/s. The solar wind exhibits a speedup throughout the heliosphere as shown by Parker (1958) [29].

The density at the inner boundary was calculated from the conservation of mass flux throughout the heliosphere as

$$\rho_0 = \frac{v_E}{v_0} \left(\frac{r_E}{r_0} \right)^2 \rho_E, \quad (7)$$

where the indices E and 0 stand for Earth and inner radial boundary respectively. The desired values of $(v_r)_E = 400$ km/s and $\rho_E = 5$ m $_p$ /cm 3 have been used here. The pressure is derived from values of density and temperature via the ideal equation of state.

The magnetic field has been set using the *Parker spiral* magnetic field model. [29] It is a simple yet very useful model to set up the basic structure of the *interplanetary magnetic field* (IMF). The solar wind plasma is in the ideal MHD regime, such that magnetic field lines are frozen into the plasma. As the Sun itself is rotating with a period of approximately ~ 27 days (~ 25 days at the equator and ~ 36 days near the poles) an Archimedean spiral structure forms. This structure has been verified by observations. [30] The model assumes the radial speed to be only a function of radius, Faraday's law and Maxwell's equation $\nabla \cdot \mathbf{B} = 0$ for a spherically symmetric geometry, leading to the explicit magnetic field components: [29]

$$B_r = B_S \left(\frac{r_S}{r} \right)^2, \quad (8)$$

$$B_\theta = 0, \quad (9)$$

$$B_\phi = -B_S \frac{\omega_S r_S}{v} \frac{r_S}{r} \sin \theta, \quad (10)$$

where the r_S is the radius of the Sun. We also take $B_S = 2.5$ G = $2.5 \cdot 10^5$ nT and the $\omega = 2.7 \cdot 10^{-6}$ rad s $^{-1}$. [31] These relations are evaluated at the inner radial boundary leading to the parameters shown in Table 1.

The polytropic index has been set to $\gamma = 1.5$, to implement the empirical value of the free streaming solar wind. [32] However it shall be noted that this still does not capture the full kinetic heating of the solar wind via a variety of electron and

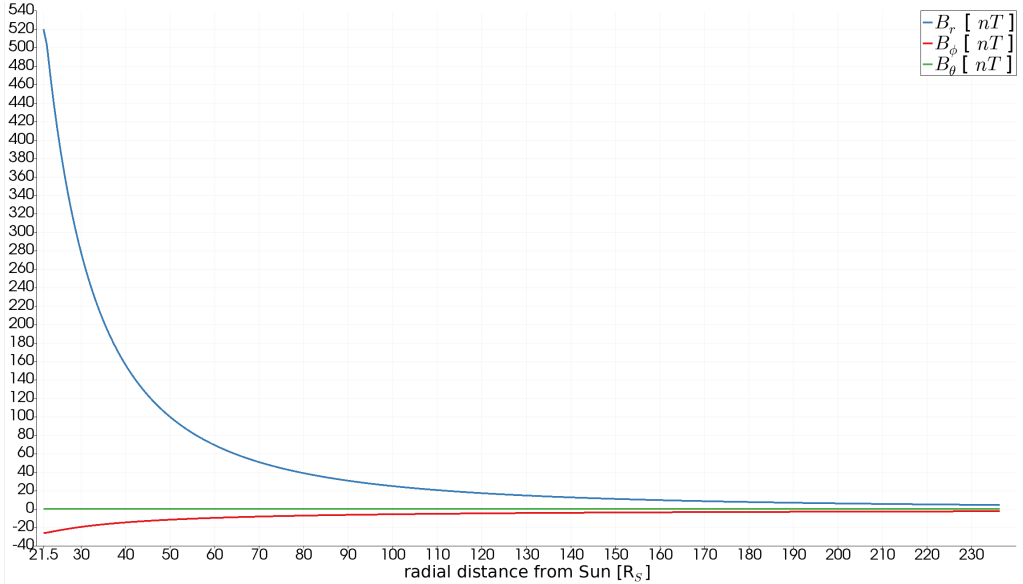


Figure 2: Radial profile of the steady-state heliosphere for the magnetic field components. Exhibits a $1/r^2$ drop of the radial and azimuthal magnetic field and an expected zero component in the polar magnetic field.

ion-scale instabilities. (e.g. [33] [34]). Thus the MHD simulations conducted here, as heliospheric MHD simulations in general, do result in a steeper radial temperature profile than the one measured in-situ. [35]

In order to establish a self-consistent solution to the solar wind and Parker spiral within the simulation domain, a simulation is set to run for 10 days. After about 7 days a steady state solution is established in the entire simulation domain. The radial profile of this steady-state can be seen in Figure 2 and 3. The steady-state values found at Earth are $v_r = 477.66$ km/s, $\rho = 4.21$ m_p/cm³, $B_r = 5.46$ nT, $B_\theta = 0.0001$ nT and $B_\phi = -2.57$ nT. These values are well within acceptable conditions for a slow solar wind. Furthermore, the resulting magnetic field structure clearly shows an Archimedean Spiral in the equatorial plane, see Figure 4. According to the theory, the Parker spiral should have a 45° angle at 1 AU ($\approx 215 R_S$) with respect to the x-axis in HEEQ coordinates, which was indeed verified.

This steady state of the heliosphere simulating a slow solar wind with magnetic field structure was taken as the initial state for all further simulations.

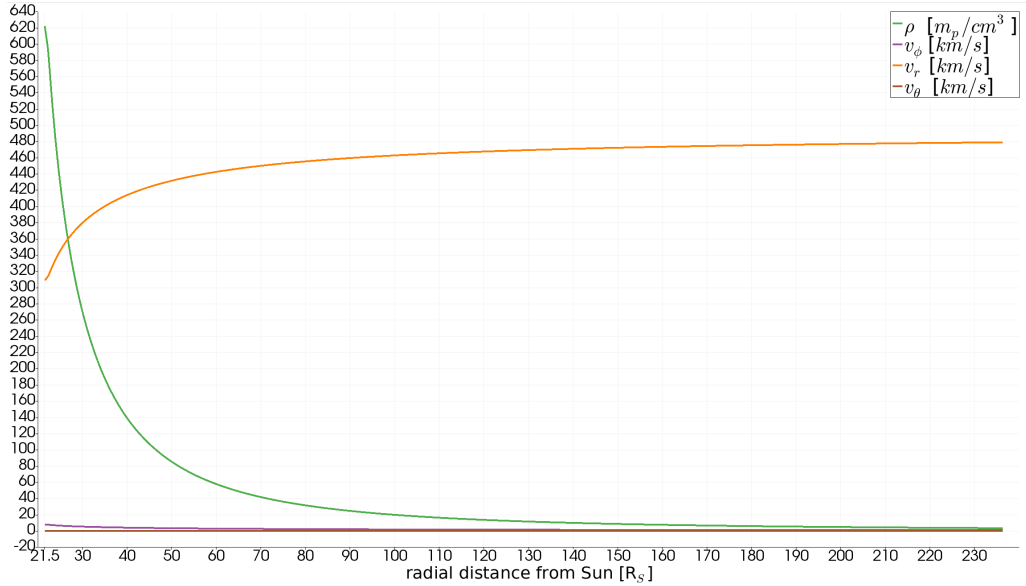


Figure 3: Radial profile of the steady-state heliosphere for velocities and density. Shows the expected $1/r^2$ decrease in density and a rapid speedup of the radial velocity to a constant value. Small, unexpected, but negligibly non-zero velocities can be seen for the azimuthal velocity close to the inner boundary.

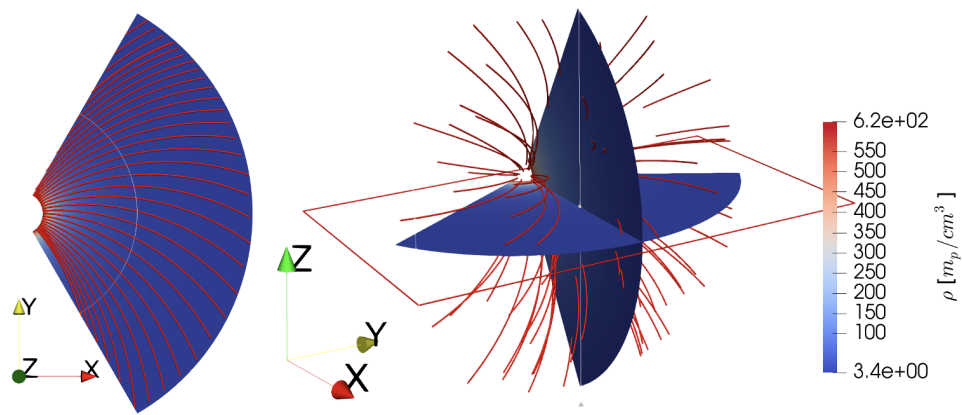


Figure 4: Slices of density profile and magnetic field lines (red) in the steady-state heliosphere. Left: Sun's equatorial plane; Right: 3D view with equatorial plane in red frame.

2.4 CME Models

Models describing the evolution of CMEs in the heliosphere can be classified into two categories: *cone* models, *flux-rope/spheromak* models. The distinctive characteristic is that the later describes CMEs with an internal magnetic field structure and cone models represent CMEs only hydrodynamically.

2.4.1 Cone Model

In the last decade, cone models have been the main model to predict the impact of CMEs on the space weather, in particular *Odstrcil et al. (2004)* [36]. In cone models solar ejecta are treated as a hydrodynamic pulse expanding by a self-similar geometry. [9, 10, 11] Represented as a hydrodynamic pulse, the CME does not contain an intrinsic magnetic field other than that of the interplanetary magnetic field, but only velocity, density and a pressure enhancement. In other words, CMEs are modeled as uniformly filled solid spheres of plasma. The pressure enhancement is initialized at the inner radial boundary at 0.1 AU of the simulation domain. The model is initialized by specifying a set of 7 parameters, defining the kinematics and geometry of the CME during its injection into the inner radial boundary. The parameters are the injection time, speed $v_{CME} = v_{3D} = v_{radial}$, direction of propagation (latitude θ_{CME} and longitude ϕ_{CME}) and angular half width at 0.1 AU. The angular half-width is implicitly used to calculate the initial radius r_0 of the plasma bubble. The density and temperature within the solid sphere are set to default values, see Table 2. The interaction of the CMEs magnetic field with the solar wind and the interplanetary magnetic field is not modeled.

Cone models have the advantage that the assumed geometry and the limited number of input parameters and a decade long fine-tuning have provided a robustness of the numerical algorithm.

The significant disadvantage is that no intrinsic magnetic field is modeled. Cone models provide estimates on arrival time, speed and density of a CME, although these parameters do impact the severity of the compression of the magnetosphere, the major factor driving a strong geomagnetic storm is the magnetic structure of a CME. [37]

2.4.2 Earlier Flux-Rope Models

To address the major flaw of cone models, lagging a description of a magnetic field, magnetohydrodynamic (MHD) models of CMEs have been developed. The intrinsic magnetic field structure of CMEs is inferred from coronagraph observations and stability arguments. Different structures have been proposed, all aiming to reproduce the typical three part structure of interplanetary CMEs. The difficulties in these models are to infer a magnetic field structure and the added complexity of simulation due the magnetic field.

An early model was proposed by *Gibson & Low (1998)* [17] with a magnetic field structure with an analytical completely self-consistent MHD solution. The model proposed CMEs to be a closed bubble, filled with a partly anchored, twisted magnetic flux rope, embedded in a background field. It was the first MHD model to reproduce the three part structure. Problems arise in this model if multiple CMEs are simulated

Variable	Explanation	Value range	Cone Model
t_0	Insertion/Injection time of CME	Any date	X
v_{CME}	Propagation speed of the CME	0...[km/s]	X
θ_{CME}	Latitude of the centre of the CME source region	-60 - 60°	X
ϕ_{CME}	Longitude of the centre of the CME source region	0 - 360°	X
r_0	Radius of the CME	0 - 21.5 R°	X
T_{CME}	Temperature of the CME	$0.8 \cdot 10^6$ K (default)	X
ρ_{CME}	Density of the CME	10^{-18} kg/m³ (default)	X
τ_{CME}	Tilt angle of spheromak	0° - 360°	
H	Handedness of the magnetic field	-1 or 1	
ϕ_t	Total toroidal flux ($\propto B_0$)	\mathbb{R}	

Table 2: Input parameters of the LFFS CME model and their usage in the cone model. Note that the temperature and density are commonly assigned default representative values and that the $v_{CME} = v_{radial}$ is a purely radial speed of the centre of the CME, equal to the observed speed in the cone model, but not in the LFFS model.

together, a frequent occurrence on the Sun, as the footprints of the CME’s flux rope stay attached to the Sun. After modifications for this issue and more by *Shiota & Kataoka (2016)* [38], further issues related to negative pressures within the CME persisted. [39]

Because of these issues *Verbek et al. (2019)* [12] and earlier models [40, 41, 38] moved to represent the intrinsic magnetic field of a CME as a *Linear Force-Free Spheromak* (LFFS). Here the solution is only partly self-consistent in MHD, which makes the simulation much more practically useful. This model allows to simulate CMEs with an approximate internal magnetic field structure and their propagation in the inner heliosphere.

2.4.3 Linear Force-Free Spheromak CME Model

A *Linear Force-Free Spheromak* (LFFS) is a force-free magnetic field configuration of spherical shape. The LFFS model uses it to represent the approximate internal magnetic structure within the central part of a CME at 0.1 AU from the Sun. If the spheromak is completely inserted in the heliosphere it will be entirely disconnected from the Sun, in contrast to the *Gibson & Low (1998)* [17] model. It shall thus be noted that empirical observations have shown that the axes of magnetic flux-rope structures in CMEs have ellipsoidal shapes often still connected to the Sun. [42] Therefore the spheromak flux-rope model is an approximation of the main frontal lobe, which is suspected to have the highest impact on space weather, yet does not capture the global, large scale geometry of an interplanetary CME. The conceptual position of the spheromak in a CME is shown in Figure 5.

A CME is initialized just as in the cone model as a solid sphere of uniform density and temperature. Additionally, an internal magnetic field structure of the spheromak is placed instead of the interplanetary magnetic field.

The spheromak model is described by additional 3 parameters in comparison to the cone model, making a total of 10, listed in Table 2. The orientation of the magnetic field is described by the tilt angle τ_{CME} and handedness H . The magnetic field strength in the spheromak is defined via the total toroidal flux ϕ_t .

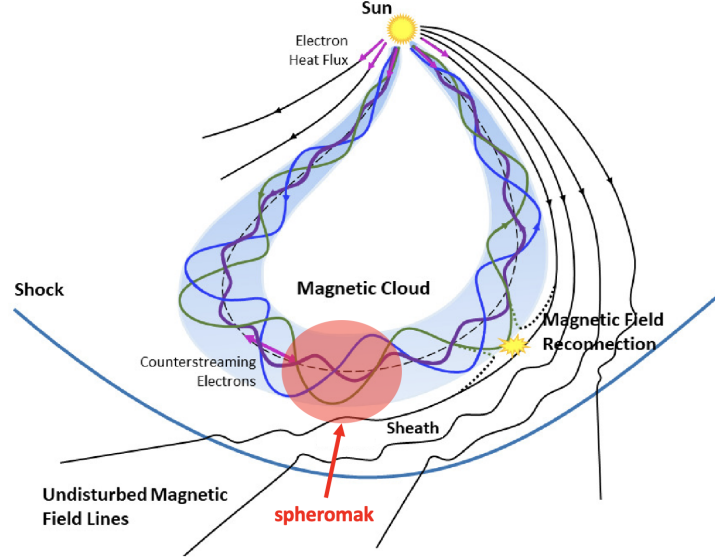


Figure 5: Cartoon showing a CMEs magnetic field structure indicating the conceptual position of the spheromak. Other effects and processes as the electron heat flux and magnetic reconnection to the interplanetary magnetic field are shown, but not discussed here. (Figure based on Wang *et al.* (2018) [43])

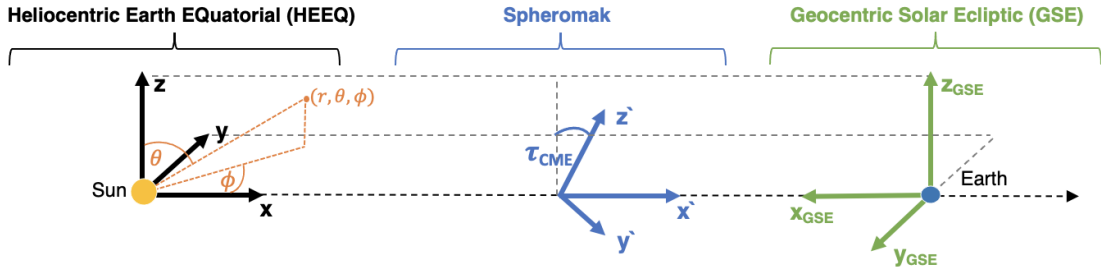


Figure 6: Illustration of coordinate systems used in simulation, spheromak modelling and analysis. Positions of Sun and Earth are indicated.

In the original model proposed by Verbeck *et al.* (2019) [12], the spheromak is injected into the heliosphere by updating the conditions at the inner boundary ghost cells to simulate a spheromak propagating into the simulation domain at a constant speed v_{CME} . In this setup the spheromak would be initialized at position $(0.1\text{AU}-r_0, \theta_{CME}, \phi_{CME})$ in HEEQ coordinates, just outside the inner radial boundary and then propagate into the simulation domain. Note that this project made a substantial change here, see Section 2.6. To determine whether a point in the simulation domain is within the spheromak, the distance between that point and the CME's centre is computed and it is required that the following must hold

$$(x_{CME} - x_{bound})^2 + (y_{CME} - y_{bound})^2 + (z_{CME} - z_{bound})^2 \leq r_0^2, \quad (11)$$

where $(x_{CME}, y_{CME}, z_{CME})$ and $(x_{bound}, y_{bound}, z_{bound})$ denote the point of the centre of the CME and the point of consideration in the cartesian HEEQ coordinates, respectively.

The magnetic field structure is defined in a local coordinate system centred on the spheromak. In this local coordinate system, indicated by primed quantities,

the magnetic field exhibits azimuthal (ϕ') symmetry, i.e. the z' axis is an axis of symmetry. In order to determine the magnetic field at a point in the HEEQ system a translation to the centre of the CME as well as a rotation of the coordinate system by the tilt angle, defined to be between z and z' axis, in the zy -plane is necessary. See Appendix C for details on the transformations.

In this local coordinate system (r' , θ' , ϕ') of the spheromak, its internal magnetic field can be defined in terms of two scalar potential functions A and Q as:

$$\mathbf{B} = \frac{1}{r' \sin \theta'} \left[\frac{1}{r'} \frac{\partial A}{\partial \theta'} \hat{\mathbf{r}}' - \frac{\partial A}{\partial r'} \hat{\boldsymbol{\theta}}' + Q \hat{\boldsymbol{\phi}}' \right]. \quad (12)$$

Here A and Q are scalar potentials dependent only on r' and θ' . [44] This magnetic field is divergence free by construction and is intended to be force-free: $\mathbf{J}' \times \mathbf{B}' = 0$. A force balance in the azimuthal direction can be obtained by requiring Q , which provides the toroidal field, to be a function of the poloidal potential A , i.e. $Q = Q(A)$. This relationship is set to be linear, giving rise to a linear force-free solution, hence the name of the model. This relationship is

$$Q(A) = H\alpha A, \quad (13)$$

where H is a dimensionless parameter, called the handedness of the spheromak, and can take values of +1 and -1 and α is a positive constant of units of inverse length. Then the solution of Equation 12 is given by the scalar potential A as

$$A = \frac{B_0}{\alpha} r' j_1(\alpha r') \sin^2 \theta', \quad (14)$$

with B_0 defining the magnetic field strength and $j_1(x)$ as the spherical Bessel function of order one, see Appendix A. Evaluating Equation 12 with Equation 14 yields the magnetic field structure of the LFFS model:

$$B'_r = 2B_0 \frac{j_1(\alpha r')}{\alpha r'} \cos \theta' \quad (15)$$

$$B'_\theta = -B_0 \left[\frac{j_1(\alpha r')}{\alpha r'} + j_1(\alpha r') \right] \sin \theta' \quad (16)$$

$$B'_\phi = HB_0 j_1(\alpha r') \sin \theta' \quad (17)$$

The magnetic field is required to go to zero at the radial boundary r_0 of the spheromak. This is imposed via the parameter α , via setting $A(r = r_0) = 0$ hence

$$j_1(\alpha r_0) = 0, \quad (18)$$

leading to $\alpha r_0 \approx 4.4934094579$ by choosing the first zero of $j_1(x)$, see Appendix A. Note that this representation of the magnetic field structure defines the magnitude of the magnetic field using the parameter B_0 . This quantity can be found from the total toroidal flux ϕ_t , see Appendix B.

As the LFFS model does contain this magnetic field structure, one additional complexity in comparison to the cone model arises. The internal magnetic field structure leads to an additional magnetic pressure inside the CME and hence a radial expansion due to this magnetic pressure. This means that the actual observed speed v_{3D}

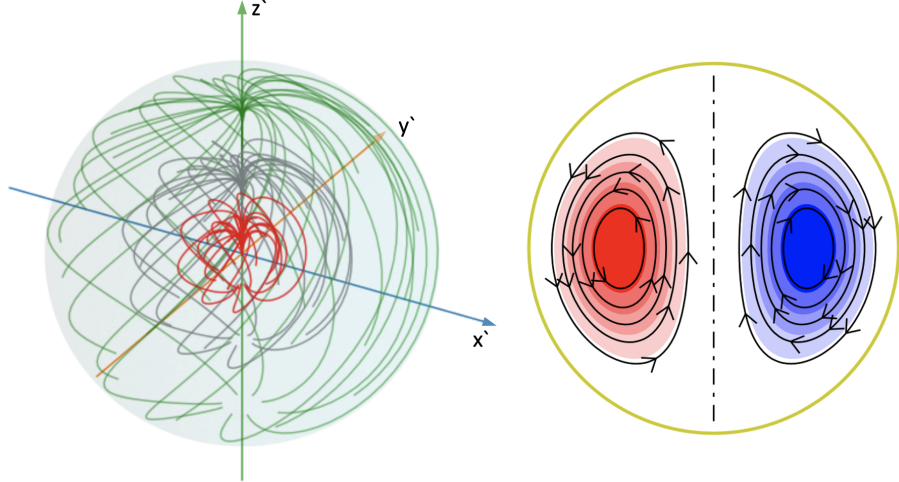


Figure 7: Left: 3D visualization of the spheromak's magnetic structure at different radii. Magnetic field lines of large radii come out of the bottom and go into in the top center with the positive z' -axis defined in the vertical. Absence of field lines at the $-z'$ -pole is due to practical difficulty in plotting.
 Right: Cross-section of spheromak in $x = 0$ or $y = 0$ plane. Black lines represent the poloidal field. Blue and red shading represents the toroidal field strength.
 Spheromak shown has handedness is $H = +1$ (Right figure from *Lyutikov et al. (2012)* [45])

of the CMEs front is a combination of the translational speed of the CMEs centre and its radial magnetic expansion, i.e.

$$v_{3D} = v_{radial} + v_{expansion}. \quad (19)$$

v_{3D} is identical with the translational speed of the centre of the CME, v_{radial} , for the cone model, but not for the LFFS model. For the LFFS model the spheromak centre is only given the transnational speed $v_{CME} = v_{radial}$, which is required to be lower than the corresponding speed of the cone model. The magnetic expansion should happen due to the internal magnetic field. Hence $(v_{radial})_{\text{Cone}} > (v_{radial})_{\text{LFFS}}$.

2.5 Verification of Stability of Spheromak

To verify the magnetic flux rope field structure and test its stability due to the requirement of it being force-free, the following test was run. The spheromak including its enhanced density and temperature region was initialized in a static uniform density and temperature environment representative of conditions at 0.1 AU. No background magnetic field or velocity were set. The aim of this test was to establish, whether the spheromak is sufficiently stable for a time period long enough to inject it into the heliosphere (few hours) and beyond at a coarse grid resolution. Eventually, a time evolution is expect, due to the finite grid resolution, and hence only approximate force-free state of the spheromak.

Figure 8 shows the spheromak shortly after initialization and after 28 h. A grid resolution of $0.5 R_s$ radial, 9° azimuthal and 4° polar was found to allow field line

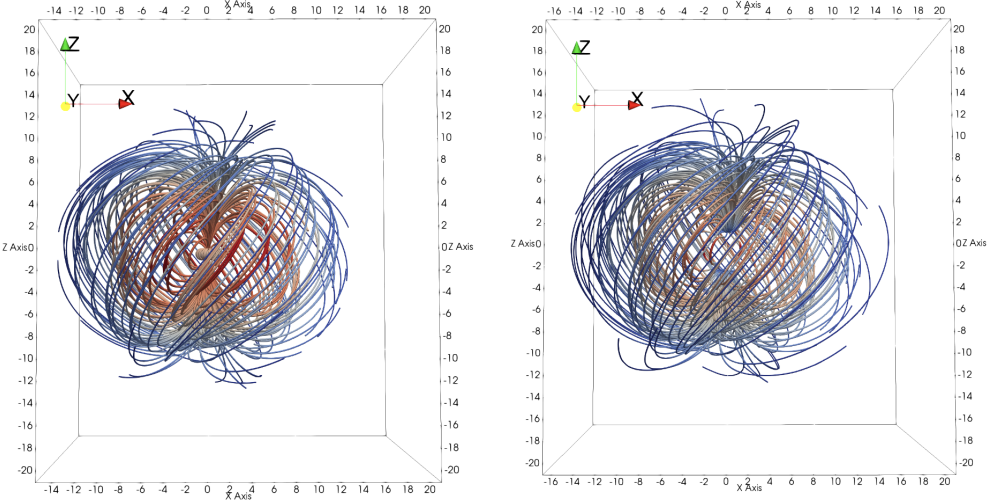


Figure 8: Approximate magnetic field structure of the initialized spheromak (left) and the spheromak after 28h of evolution (right) in uniform density, representative of conditions 0.1 AU - no background magnetic field or velocity. Red to blue coloring denotes increasing magnetic field strength. Magnetic field lines ending or diverging from the spherical extend are due to the low simulation grid resolution. ($r_0 = 15 R_s$, $H = +1$) Figure made in ParaView.

tracing using linear interpolation and a second order Runge-Kutta tracer in the ParaView software. The plotting of individual field lines was also shown to be viable at lower resolutions of $0.7 R_s$, as chosen for the final simulations.

Firstly, this test verified the approximate structure of the spheromak, as shown in Figure 7, up to sampling issues of the field line plotting and some few diverging field lines. Secondly, it was shown that the evolution of the spheromak over the more than sufficient time period of 28 h is small. Hence, the spheromak is still approximately force-free at this grid resolution as required.

2.6 Injection/Insertion of the Spheromak in the Heliosphere

The final step in the simulation development was to establish how to place the spheromak into the heliospheric simulation domain.

Just as in the cone model, the LFFS model proposes to inject the spheromak into the simulation domain by imposing dynamic boundary conditions on the inner radial boundary at 0.1 AU. On initialisation the spheromak centre is just outside the inner radial boundary at $(0.1 \text{ AU}-r_0, \theta_{CME}, \phi_{CME})$ in HEEQ coordinates. At each time step of the simulation the spheromaks new position is evaluated based upon the constant radial speed, v_{CME} , it was initialised with. The ghost cells at the inner radial boundary are updated in accordance, so that the spheromak enters the simulation domain at the specified velocity.

2.6.1 Difficulties with Injecting

The method to inject the spheromak revealed itself to be infeasible using the PLUTO environment. Initially, a simple 1 cell layer ghost cell boundary was imposing the

dynamic boundary conditions. During the injection of the spheromak nonphysical negative pressures were consistently measured. This is a common issue in MHD codes and arises due to the fact codes like PLUTO update the total energy, so that the pressure is just a derived variable. In certain situations the pressure can be several orders of magnitude smaller than either the kinetic energy or the magnetic energy. Therefore small discretization errors in the total energy can lead to negative gas pressures. [46] As time steps are dynamic in PLUTO according to conditions of stability, (see *Mignone (2007)* [27] and [47] for details), negative pressure lead to smaller time steps. This issue lead to unpractical simulation times. The probable cause is that the already injected part of the spheromak is evolving in the domain with the solar wind such that in some regions the magnetic field lines lead to mass being expelled back into the inner boundary.

Further attempts were made to inject the spheromak with a more sophisticated inner boundary. This time the spheromak's values where set not just at the 1 cell layer of ghost cells, but also in all cells within $8.5 R_s$ of the inner boundary. Also this implementation lead to the same negative pressure issues.

A practical preventive measure that many MHD simulations apply is to set a lower bound on the pressure. Unfortunately, the negative pressure issue proved to be too rapidly evolving for this to solve the issue.

To the current state of the published literature, the LFFS model has only been successfully implemented in the EUHFORIA (EUropean Heliospheric FORcasting Information Asset) [48] simulation code by *Verbeke et al. (2019)* [12] and *Scolini et al.* [13]. A modified version of the spheromak was also implemented in the Multi-Scale Fluid-Kinetic Simulation Suite (MS-FLUKSS) [49] by *Singh et al. (2020)* [14]. These advanced MHD codes may implement more sophisticated adaptive grids resolutions and advance inner boundaries to address named issue.

2.6.2 Inserting the Spheromak and its Implications

Since the injection of the spheromak had been proven to be infeasible in the PLUTO code, it was chosen to insert the spheromak such that it is initialized just inside the inner boundary hence at $(0.1 \text{ AU} + r_0, \theta_{CME}, \phi_{CME})$ in HEEQ coordinates. The setup can be seen in Figure 9.

This method is still a reasonable implementation to the capture evolution of CMEs qualitatively. Spheromaks of small extend, $r_0 \lesssim 10 R_S$, should be chosen, such that they don't extend to far into the heliosphere upon insertion. At first thought it may seem surprising one would not just shift the inner boundary closer to the Sun, such that the spheromak can be inserted at the correct position. Yet even small spheromaks of sizes $r_0 \lesssim 10 R_S$ would reach very close to the Sun where simulations would be infeasible due to the high magnetic field of the solar wind. Furthermore, the spheromak should not be thought of as the approximate CME structure at $r = 0.1 \text{ AU} - r_0$, but rather as the emergent structure after it moved to 0.1 AU. This becomes obvious if one imagines spheromaks of initial radii of $r_0 \gtrsim 15 R_S$.

The parameters needed to specify the spheromak structure, listed in Table 2, have been estimated for a handful of CME events from remote satellite observations in multiple papers (e.g. [13] [12]), yet it shall be noted that this is a newly emerging field. The parameters can be found for spheromaks injected through the inner boundary. This raised the question what parameters to use for inserting a spher-

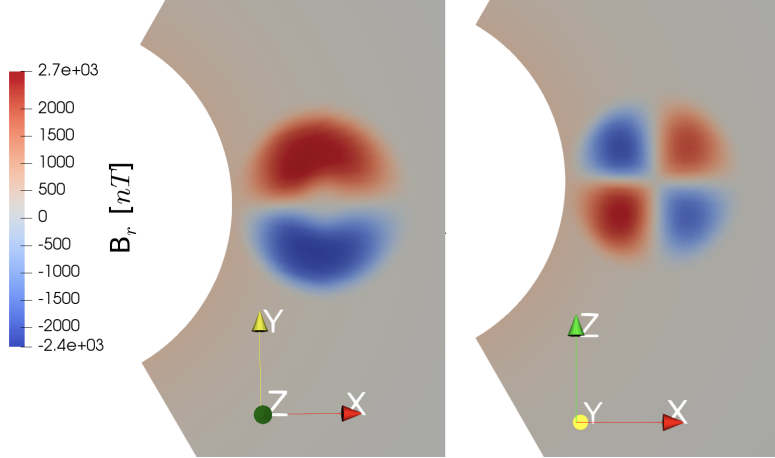


Figure 9: Slices of B_r in HEEQ coordinates of spheromak inserted in the simulation domain close to the inner boundary on initialization. Left panel shows the $z = 0$ and right panel the $y = 0$ plane. Spheromak has $\tau = 180^\circ$ and $H = +1$.

mak about $2 r_0$ afar.

For that matter a scaling of CME size dependent parameters, in particular r_0 and B_0 or ϕ_t , was attempted. The time it takes for the CMEs centre to reach the new position ($0.1 \text{ AU} + r_0, \theta_{CME}, \phi_{CME}$) was calculated based on the translational velocity v_{radial} only. Then as both LFFS and cone model assume that initially CMEs expand by self-similar geometry it was attempted calculate the larger radius r'_0 of the spheromak at the new position from the magnetic expansion speed $v_{expansion}$. The method proved to lead to unreasonably large CMEs, due to missing drag forces and was abandoned.

Instead this project proceeded by choosing real estimated values, meant for the injection of the spheromak of a small CME. Choosing small CMEs should mitigate the impact of the shorter distance to Earth. This means that absolute values in the outcome of the simulations of this project should be considered with care, which is not very consequential as this is a parametric study, aiming for qualitative conclusions.

It must be noted that even the insertion of the spheromak lead to negative pressure warnings shortly after the initialization, yet these were transient and much less severe. The overall dynamics of the systems appear physical, so this flaw in the model can be regarded as minor.

2.7 Initialization of Internal Magnetic Field

An important detail of the novel spheromak model proved to be not well documented in the published literature at the time of writing this. No statements were made whether the internal magnetic field structure of the spheromak should be set instead of the background magnetic field of the Parker spiral or on-top of it. The spheromaks magnetic field goes to zero at its boundary, thus to avoid discontinuities in the total magnetic field, setting the spheromak's magnetic field on-top of the interplanetary magnetic field was favoured initially. *Stage 1 & 2* of the parametric study, see Section 3, use this method. Later in this project, it was realized that CMEs are expelled as closed magnetic structures from the Sun - closed off from the solar wind

magnetic field. *Stage 3* of the parametric study thus employs the method of setting the internal magnetic field of the spheromak instead of the interplanetary magnetic field.

Various test simulations were run to investigate the impact of this inconsistency in the method. Despite relatively large initial difference in the magnetic field close to the Sun, no significant difference can be measured at the Earth's position. This puts no restrictions on the results obtained in *Stage 1 & 2* of this parametric study.

2.8 Virtual Spacecraft

In order to examine the potential impact of the CME caused disturbance to the solar wind at Earth, a virtual spacecraft was placed at 1 AU distance to the Sun on the x-axis in HEEQ coordinates. It is merely a data logger recording the solar wind conditions at Earth's position without the magnetosphere present.

3 Parametric Study

The novel LFFS model for the first time allows to, at least approximately, model the magnetic behaviour of a CME, propagating through the inner heliosphere. This opens the door to an entire new set of dynamics. Earlier papers have already attempted some parametric studies with the LFFS model, exploring the single CME dynamics and showing that CME-CME interactions result in realistic predictions. [14] Here the interactions of CMEs will be investigated by varying the tilt angle, waiting time and handedness in this order for the following reasoning:

To limit the size of the parameter space this study was conducted in three stages, each time choosing the probably most geoeffective case and moving to the next stage. The base scenario has been chosen to be a single or two CMEs propagating on the x-axis in HEEQ coordinates, such that a direct hit of Earth could be investigated. As the main advantage of the LFFS model is the internal magnetic field structure, it appeared obvious to investigate the impact of a single spheromaks orientation on the geoeffectiveness first. For that matter the tilt angle was chosen to be varied in *Stage 1*. It is the main handle of setting the orientation of the spheromak with respect to the HEEQ z-axis. Once the most geoeffective orientation is identified, the main stage, *Stage 2*, would proceed with that orientation to simulate CME-CME collisions. The parameter varied here would be the waiting time between inserting the CMEs. Lastly, the most geoeffective waiting time would be fixed, to vary the handedness of the spheromak in *Stage 3*, in order to explore the magnetic interaction between two CME in depth.

This choice of parameter space allowed to study the most interesting new features of the CME model in regard to CME-CME interactions. The exact parameters for both CMEs in terms of initial radius r_0 and ϕ_t (i.e B_0) were set to represent two CMEs of the same size, based on real observations, yet setting different fixed velocities.

3.1 Input Parameters of Spheromak

The input parameters for the LFFS model are constrained from remote-sensing observations of CMEs and their sources region on the Sun. Only a handful of papers have so far attempted the estimation of these parameters due to the novelty of the LFFS model and no standard methodology seems to be established yet. (e.g. [13] [12]) The purpose of this section is to explain the choice of parameters made for the parametric study. For context only a brief mentioning of how these parameter are estimated will be made prior.

The kinematic and geometric parameters are estimated from multiple satellite observation that are being fitted to a croissant-like 3D shape, using a cylindrical shell model. The observed speed can be found from a time series of such a model, giving the v_{3D} velocity. The separation of this observed speed into an expansion and radial speed of CMEs is non-trivial and subject to theoretical models.

The estimation of magnetic parameters has been described as extremely challenging and is only possible with strong approximations combined with photospheric and coronal observations of the source active region before and after the eruption. [13]

	Variable	CME0	CME1
	Insertion time of CME [in h]	0	12-36
Initial position	Initial radius r_0 [in R_S]	10.5	10.5
	Radial r_{CME}	0.1 AU + r_0	0.1 AU + r_0
	Polar θ_{CME}	45°	45°
Velocity	Azimuthal ϕ_{CME}	0°	0°
	Total v_{3D}^\dagger [in km/s]	723	1723
	Radial v_r [in km/s]	500	1500
Magnetic field	Magnetic expansion v_{exp}^\dagger [in km/s]	223	223
	Field strength B_0 [in nT]	1400	1400
	Tilt angle τ_{CME}	0-270°	0-270°
	Handedness H	+1 (or -1)	+1 (or -1)

Table 3: Parameters chosen as the base CME for LFFS model in this paramedic study. Parameters in light grey cells are fixed throughout the study. Parameters in bold have been adapted directly from observational estimations by *Scolini et al. (2019)* [13] for realistic modelling. All plain cells are varied throughout *Stages 1-3*. The dagger indicates a derived quantity not directly inputted, i.e. implied by other parameters.

The choice of parameters made for this parametric study is based on the estimation made by *Scolini et al. (2019)* [13] for the CME-CME event recorded on the 13/14 June 2012. It is one of the few CME-CME interaction events with estimations for the LFFS parameters at the time of writing this. Initially, it was attempted to recreate the situation up to the position of the CMEs. This however proved to be infeasible due to the failure to inject the spheromak through the inner boundary, and hence the insertion of the spheromak putting a limitation on the size of CMEs to be simulated. The choice was made to inject two small, identical CMEs of different velocities one after another. The intention was to set a very high velocity event, thought to create a high geoeffectivness. The first CME, hereafter referred to as *CME0*, would be given a radial speed $v_{radial} = v_r = 500$ km/s and the second CME, hereafter referred to as *CME1*, would be given a radial speed of $v_r = 1500$ km/s. These speeds would correspond to propagation speeds of the front of the CME of 723 km/s and 1723 km/s respectively. These velocities are well within realistic values for extreme CME events.

To ensure a realistic structure of the spheromak the magnetic strength B_0 and the initial radius r_0 were adapted from *Scolini et al. (2019)* [13] from the 13 June 2012 event. A detailed summary of the parameters chosen for this parametric study can be found in Table 3.

3.2 Quantifying Geoeffectivness

This subsection introduces a method for the quantification and classification of geomagnetic storms along notable real events for context.

The classification of geomagnetic storms is often done using the *Disturbance storm time* (Dst) index along with other indices. The Dst index is a measure of a particular westward current in the magnetosphere capable of inducing magnetic disturbance on the ground, as mentioned in the introduction. It is often referred to as just Dst. Table 4 shows the classification commonly applied and the potential impact on our

Storm class	Dst _{min} range	Impact: Powers systems; Spacecraft operations
weak	-30 to -50 nT	weak fluctuations; minor impact
moderate	-50 to -100 nT	voltage alarms in high latitude systems, long duration storms may cause transformer damage; corrective action for spacecraft orientation and drag predictions
strong	-100 to -200 nT	voltage corrections required; surface charging on satellites and increased drag in low Earth orbit satellites
severe	-200 to -350 nT	widespread voltage control problems and some protective systems may mistakenly trip out key assets from the grid; surface charging and tracking problems, orientation corrections needed
great/extreme	< -350 nT	transformer damage, widespread voltage control and protective systems problems, complete collapse or blackout of grids; extensive surface charging, orientation and up-/down-link problems

Table 4: Geomagnetic storm classification and their potential impact. Classification suggested by *Gonzales (1994)* [37] and impact estimates from *NOAA* [50])

infrastructure for context.

Two CME events and their associated geomagnetic storms should be mentioned here for later reference. The 13/14 June 2012 event, which provides the base LFFS model parameters for this parametric study, consisted of two subsequent CME events, separated by 19 h at the Sun's surface. The CMEs were ejected with observed velocities of 719 km/s and 1213 km/s respectively and achieved a maximum speed of 573 km/s at Earth and a minimum Dst of -86 nT. Note however that this CME-CME interaction did not hit Earth head on. A direct comparison to this study is therefore not applicable. The second event to be mentioned here, is the most extreme event on record, the 1859 Carrington event. Here the CME (or CMEs) transversed from Sun-Earth in 17.5 hours reaching a top speed of 2380 km/s at Earth and an estimated minimum Dst of -1760 nT. [19]

To estimate the Dst index, this project used the empirical relationship proposed by *Wu (2005)* [51]. It allows to estimate the Dst index based only on the southward interplanetary magnetic field component and the solar wind velocity. This empirical relationship is based on measurements of 135 magnetic clouds. It is written as:

$$Dst_{min} = -16.48 - 12.89 \cdot (v \cdot B_s)_{max}, \quad (20)$$

where $v = v_r$ is in HEEQ coordinates and B_s denotes the southward component of the interplanetary magnetic field capped at zero. ($B_s = |(B_{GSE})_z|$ for $(B_{GSE})_z < 0$ and $B_s = 0$ for $(B_{GSE})_z \geq 0$). Note that this cap of Dst is just required for this relationship. The Dst can be positive, yet cannot be estimated with this relationship in the positive regime. It shall be mentioned here that this relationship has been found to have an error of less than 10% for magnetic cloud regions, yet larger errors of 0-280% for sheath regions. Thus for this project it shall only be considered for the magnetic cloud itself. Nevertheless, the note that the relationship in Equation 20 is linear with respect to solar wind velocity and southward magnetic field and hence can still be used for qualitative statements in sheath regions.

Signature	Description
B1: B Rotation	$\gg 30^\circ$,smooth
B2: B Enhancement	10 nT
B3: B Variance decrease	
B4: B Discontinuity at ICME boundaries	
B5: <i>Magnetic clouds</i>	B1, B2 and $\beta < 1$
P1: Declining velocity profile/expansion	Monotonic decrease
P2: Extreme density decrease	$\leq 1 \text{ cm}^{-3}$
P3: Temperature decrease	$< 6 \cdot 10^4 \text{ K}$
P4: Upstream forward shock/"Bow shock"	Rankine-Hugoniot Relations

Figure 10: Selection of in-situ signatures of ICMEs (description applies to ~ 1 AU heliospheric distance) in the magnetic field (B) and in the plasma dynamics (P). (based on Zurbuchen *et al.* (2006) [22] and references therein)

3.3 ICME Signatures & Verification of Model

This subsection aims to provide a basic understanding of the signatures of interplanetary CMEs and their magnetic structures in spacecraft time series data. On this foundation the first single CME run is verified to show the expected signatures.

A necessary and sufficient condition to identify ICMEs in spacecraft data has not been established and it most likely unattainable. [22] Most CMEs share a common set of features in their time series, yet some CME miss some entirely. The most practical approach is to find a consensus of most signatures in a time series. A clearly defined subset of CMEs with distinct signature is called *magnetic clouds*. Magnetic clouds (MCs) have enhanced magnetic fields ($> 10 \text{ nT}$) that rotate slowly through a large angle, low proton temperature and low plasma β (ratio of the thermal and magnetic field energies). CMEs that miss some of these features are termed *complex ejecta*. [22] [52]

Ahead of fast CME, exceeding magnetosonic speed in the solar wind, fast forward shocks are generated, as shown in Figure 1. These regions usually exhibit an abrupt rise in density, velocity and an enhanced magnetic field due to the compression of magnetic field lines. These turbulent sheaths ahead of CMEs have highly variable magnetic fields and commonly a high thermal energy. i.e. large plasma β .

The actual CME signature can be distinguished from the shock best by a decrease in variability of the magnetic field. Inside of most ICMEs the magnetic fields do vary smoothly. The solar wind speed often shows a monotonic decrease alongside a decrease of the number density as far as $\leq 1 \text{ cm}^{-3}$, due to the expansion of the CME in the propagation. The temperature inside the shock and CME can have a discontinuity to the solar wind due to the separation of the CME region by closed magnetic field lines. Thus the temperature inside the CME evolves separate to that of the solar wind and can show large variations. These large variations can only be sustained in the propagation of the CME as the magnetic energy is higher than the thermal energy, i.e. $\beta < 1$. [22] [52] These features are listed in Table 10 for reference. More features of CMEs connected to plasma composition, waves and suprathermal particles are not discussed here, as they were not modeled. A full list of ICME signatures can be found in Zurbuchen *et al.* (2006) [22].

To verify the model developed in this project a single CME run has been analysed in detail for morphology, previously described signatures and a *Minimum Variance*

Analysis (MVA) has been performed. A minimum variance analysis provides an estimate of the orientation of a flux rope at 1 AU. Note that a spheromak itself is made of closed flux ropes.

The CME simulated here is the slow CME0, as defined in Table 3, with a tilt angle $\tau = 180^\circ$ and handedness $H = 1$. The virtual spacecraft timeseries are shown in Figure 12 and a timeseries of selected profiles in Figure 11.

The latter clearly shows the expected three part structure typical for normal CMEs. The density can be directly related to the brightness of the CMEs features, as mentioned earlier. Comparing the coronagraph observations in Figure 1 (left) on this basis with the profile timeseries, allows to identify all three features. Frames 15-45 h in the profile timeseries show the bright, high density core followed by the dark cavity as a low density region in the centre of the CME. The frontal bright loop is again shown by the crescent moon shaped high density region. The successful reconstruction of the typical morphology of interplanetary CMEs marked an important step to verify the model.

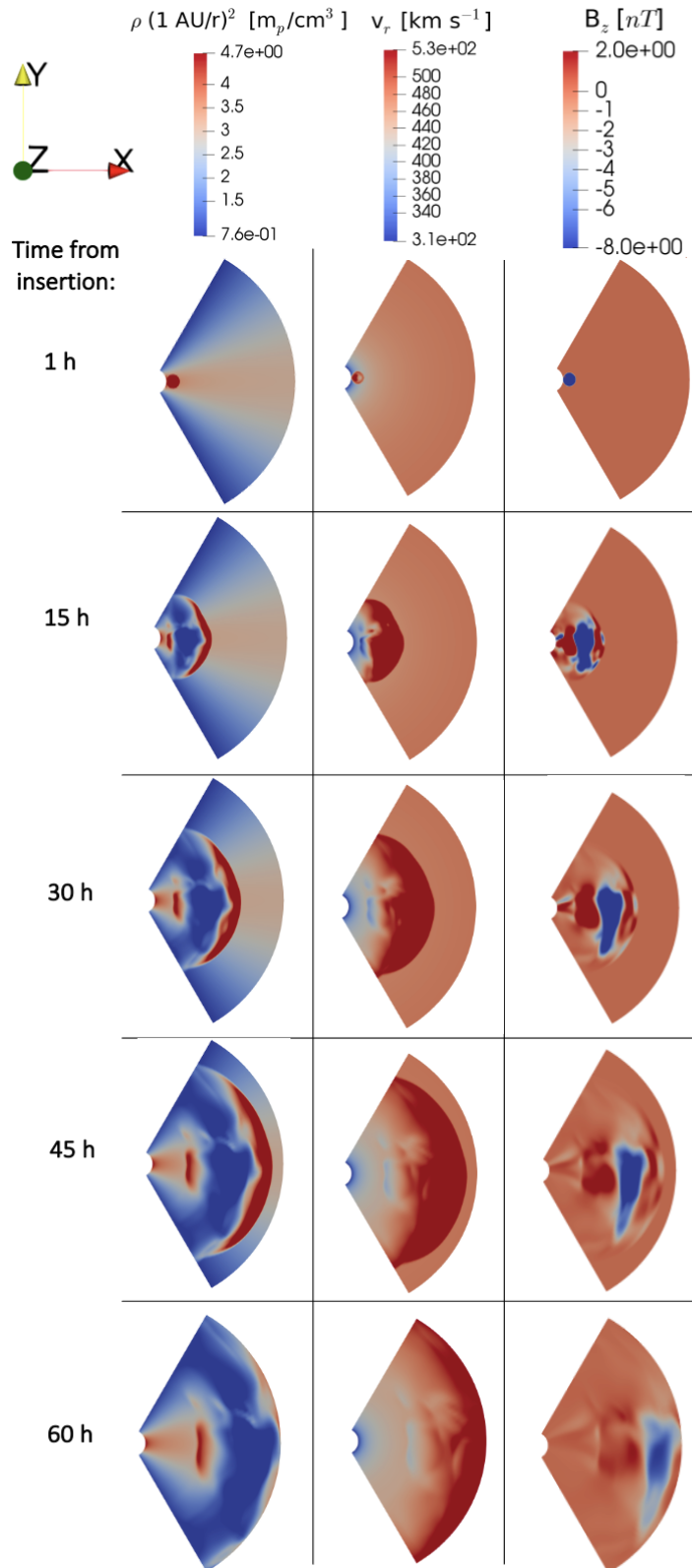


Figure 11: Timeseries of z-plane profiles of normalized density (left), radial velocity in HEEQ system (middle) and $(B_{GSE})_z$ component for CME0 of tilt angle $\tau = 180^\circ$ and handedness $H = +1$. Frames 15-45 h for density clearly show the typical three part structure of ICMEs. Note that the minor azimuthal asymmetry in the density along the x-axis is due to the grid granularity of the simulation and is only noticeable due to the normalization. It doesn't have a significant impact on the relevant results.

The virtual spacecraft timeseries clearly shows an initial shock followed by an expected CME signature, that temporarily even satisfies the criteria of a magnetic cloud. At time ~ 42 h the shock ahead of the CME reaches the virtual spacecraft placed at 1 AU, leading to the rapid increase in density, velocity and hence a high dynamic pressure. Further, the magnetic field components show a compression of magnetic field lines, presumably from the Parker spiral in the solar wind in that initial shock. The approximate separation of shock and CME is at ~ 51 h, as there the variance of the magnetic field decreases and the density falls off to a very low depression below the solar wind normal. The radial velocity shows a constant decrease due to the expansion of the CME with some minor variation, probably due to the internal magnetic field structure of the CME. Regarding the temperature, a special side note has to be made. The solar wind experiences some kinetic heating that is not yet understood, as mentioned in Subsection 2.3. Thus the equilibrium temperature profile of the solar wind modeled here is steeper, resulting in a lower temperature at 1 AU than observed. Even though the temperature outside the CME may thus be not realistic, the temperatures within the CME evolve mostly separate due to the magnetic field lines being closed off, and thereby may be analysed without restrictions. Inside the CME the temperature measured is of the right order of magnitude (10^{4-6} K) and exhibits sharp features.

The magnetic field inside the CME varies slowly and shows some rotation. A rotation may be recognised as the decrease in one magnetic field component being compensated by the other two without variation of total magnitude.

The CME even exhibits a plasma beta below unity, $\beta < 1$, between 62 h and 74 h, hence plasma motion is dominated by the magnetic field in that region. This completes the definition of a magnetic cloud.

The Dst shows a significant depression in the region of the CME and reaches a moderate minimum of -63 nT, as expected for a single slow CME. This event may be classified as a moderate geomagnetic storm.

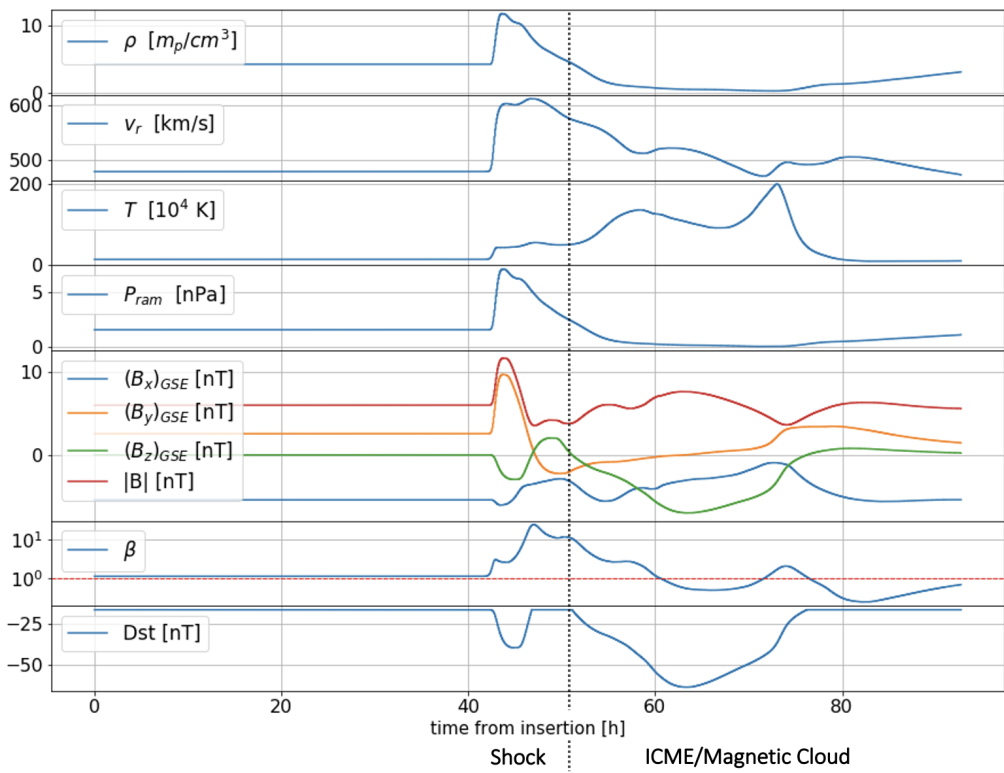


Figure 12: Virtual spacecraft data at 1 AU for CME0 of tilt angle $\tau = 180^\circ$ and handedness $H = +1$. Shows all modeled signatures of ICMEs B1-4, P1-4 from Table 10.

Boundaries		Eigenvalues			Eigenvalue ratios		Flux rope axis	
start time [h]	end time [h]	λ_1	λ_2	λ_3	$\frac{\lambda_1}{\lambda_2}$	$\frac{\lambda_3}{\lambda_2}$	θ	ϕ
47.24	76.56	8.41	2.80	0.71	3.01	0.25	-18.08	126.28
49.52	74.05	6.38	1.92	0.32	3.32	0.16	-31.10	146.89
50.66	74.05	5.15	1.90	0.20	2.71	0.11	-37.06	141.47

Figure 13: Results of Minimum Variance Analysis (MVA) of three slightly different temporal boundaries of the ICME. The third is the most favoured boundary. θ and ϕ are in HEEQ coordinates. (MVA performed by Dr. Emma Davies)

To further understand the propagation of the CME and verify the existence of a flux rope at 1 AU a Minimum Variance Analysis (MVA), as presented by *Siscoe & Suey (1972)* [53], was performed, to estimate the orientation of the spheromak. The technique can be performed on both the sheath region and the magnetic flux rope or spheromak. It involves calculating the eigenvectors and eigenvalues of a covariance matrix of the magnetic field components. When a MVA is applied to a flux rope (spheromak), then the intermediate eigenvector corresponds to the direction of the flux rope axis (z-axis). The orientations are well defined if $\frac{\lambda_1}{\lambda_2} < 1.37$ and $\frac{\lambda_3}{\lambda_2} < 0.72$, as defined by *Siscoe & Suey (1971)* [53]. Table 13 shows the results of the MVA for different temporal ranges. The analysis suggests that the spheromaks z'-axis has the orientation of ($\theta = -37.06^\circ$ (142.94), $\phi = 141.47^\circ$ (-37.53)) up to an 180° ambiguity due to the MVA itself. This means that the spheromak, initially of orientation ($\theta = 180^\circ$, $\phi = -90^\circ$), underwent a moderate rotation during its passage from Earth, which is not uncommon for CMEs.

This in depth analysis of morphology, timeseries signatures and MVA of the single CME0 event of tilt $\tau = 180^\circ$ and handedness $H = +1$ shows all features, expected to be captured by the model developed here. This can be seen as sufficient verification of this model.

3.4 Stage 1: Tilt Angle

The first stage of the parametric study was chosen to vary the tilt angle of a single spheromak, as it is the main handle of its magnetic orientation. Preliminary runs had shown that different tilt angles can produce vastly different magnetic signatures at Earth, most importantly some with strong positive or negative southward magnetic field. The objective was to identify the most geoeffective single CME tilt angle. For that matter 4 simulations were run of tilt angles $\tau = 0^\circ, 90^\circ, 180^\circ, 270^\circ$ with fixed handedness $H = +1$.

The general discussion of the CME signatures has already been made for the $\tau = 180^\circ$ run in the previous Subsection 3.3. All runs show the main signatures B1-3, P1-4, as listed in Table 10. Here the focus of the analysis is on the individual magnetic field components in the virtual spacecraft data in Figures 14, 15, 12 and 16. The magnetic field structure of the spheromak is strongly deformed in the propagation from Sun to Earth, yet the magnetic field direction of the initial spheromak in the z'-axis can still be recovered at 1 AU.

For the $\tau = 0^\circ$ tilt run the spheromak is inserted in upright orientation as shown in Figure 7 with the positive z'-axis of the spheromak aligned with that of the HEEQ system. Thereby, one would expect the main direction of the magnetic field lines

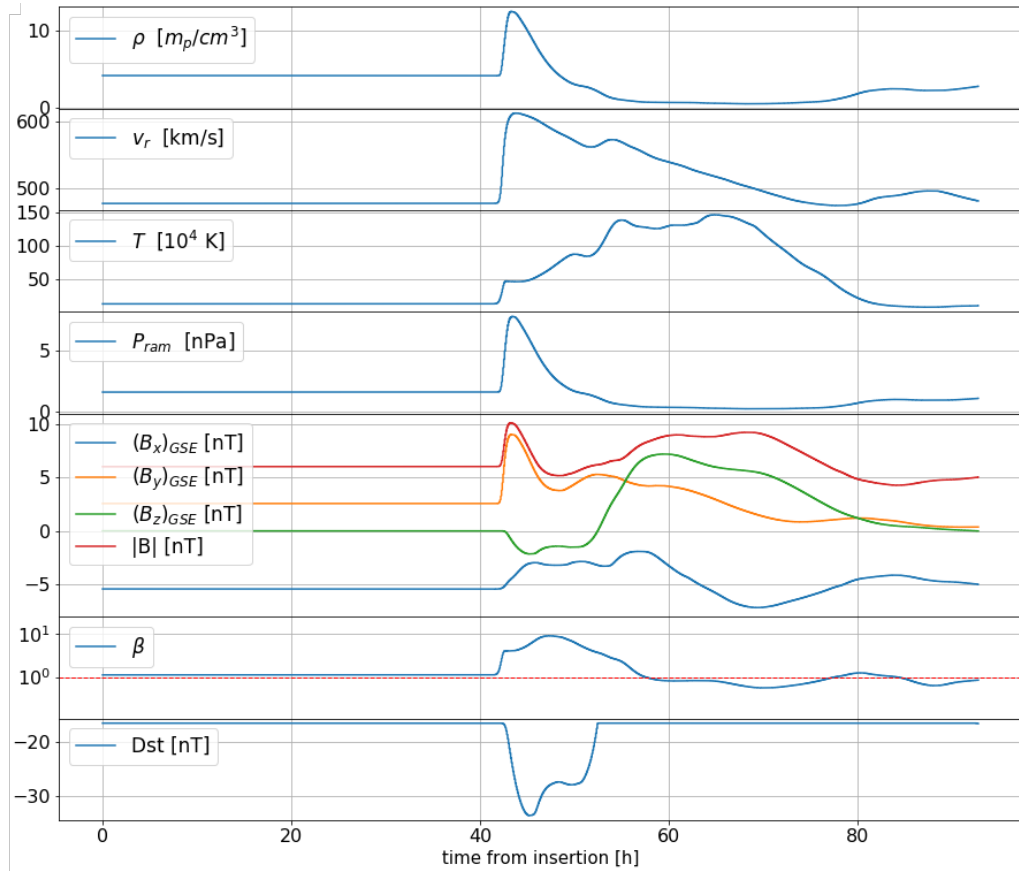


Figure 14: Virtual spacecraft data at 1 AU for a CME0 tilt angle $\tau = 0^\circ$.

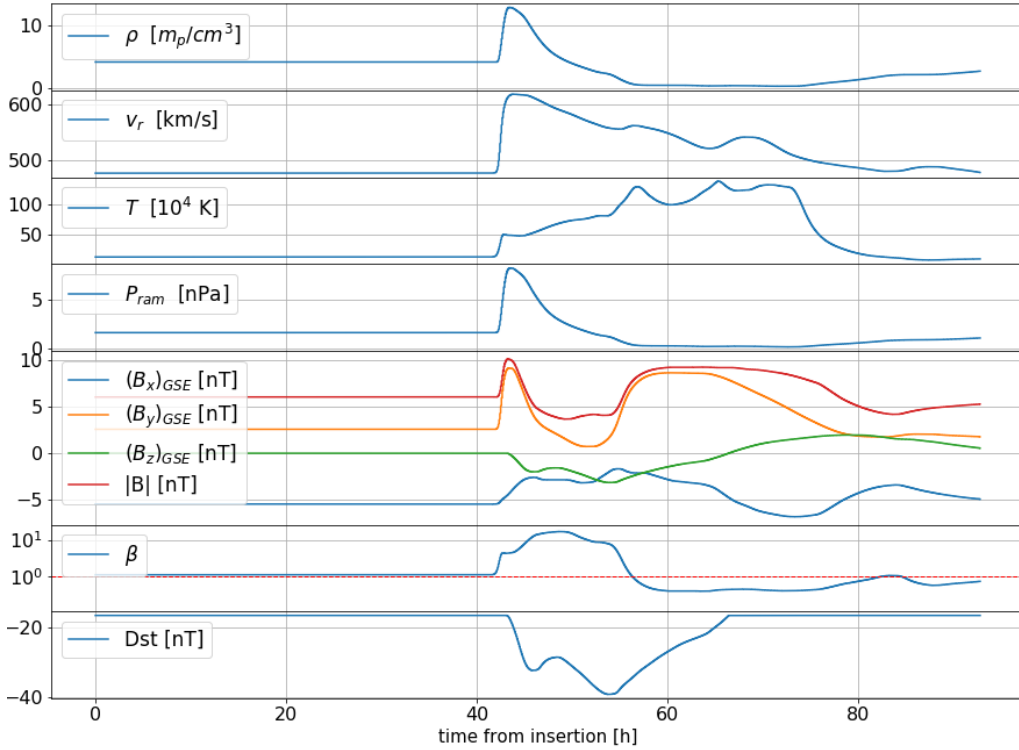


Figure 15: Virtual spacecraft data at 1 AU for a CME0 tilt angle $\tau = 90^\circ$.

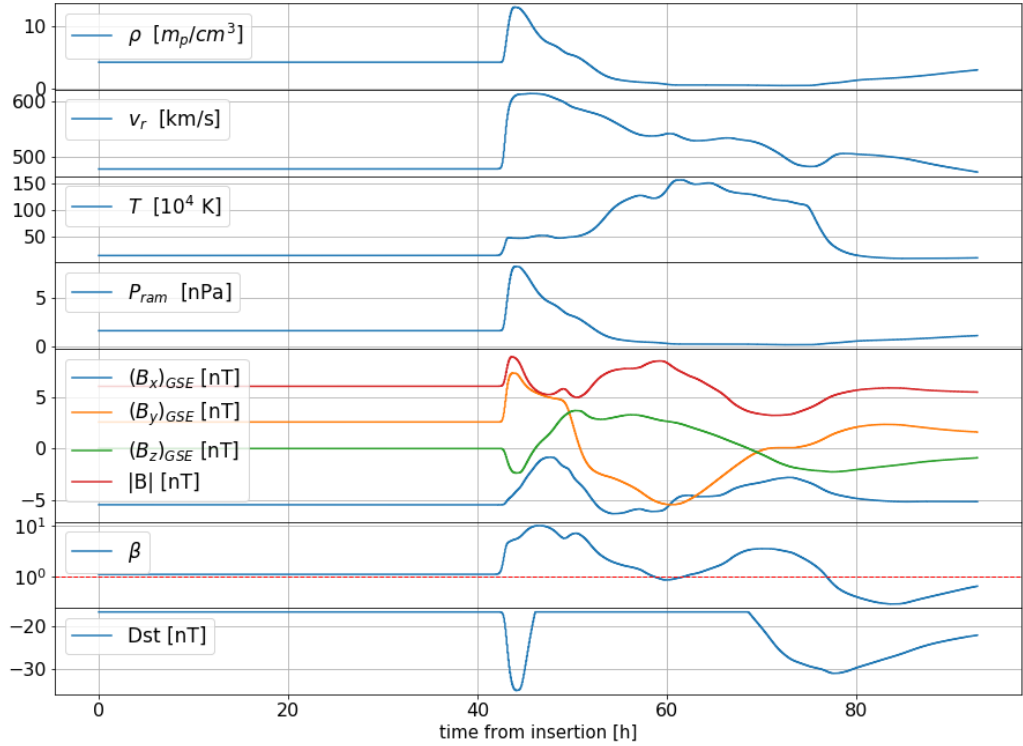


Figure 16: Virtual spacecraft data at 1 AU for a CME0 tilt angle $\tau = 270^\circ$.

to be in the positive z-direction apart from the very centre of the spheromak. A strong positive $(B_{GSE})_z$ component is indeed observable in the virtual spacecraft timeseries between 54 h and 80 h. Even the $(B_{GSE})_x$ component can be identified to undergo a rotation from positive to negative, as expected as it corresponds to the radial component in inside the spheromak. The $(B_{GSE})_y$ component however does not obviously relate the spheromaks structure at 0.1 AU.

As the only contribution to the southward component of the magnetic field at 1 AU is due to the shock ahead of the CME, reaching only a Dst of -33.50 nT and only for a short duration of ~ 9 h, this event would be classified as a weak geomagnetic storm.

For the $\tau = 90^\circ$ tilt run the spheromak is inserted with the positive z' -axis of the spheromak aligned with the y-axis of the HEEQ system. Here the main direction of the magnetic field lines at insertion is now in the negative y-axis. The $(B_{GSE})_y$ component within the ICME region does agree with this expectation, but shows a negative to positive rotation. The $(B_{GSE})_z$ component however shows a mild rotation from negative to positive, as is expected for the first and second half of the spheromak of handedness $H = +1$.

This mild depression in the southward component of the magnetic field lead to a Dst of -39.1 nT, classifying this event as a weak geomagnetic storm.

The $\tau = 180^\circ$ tilt run, discussed earlier, inserted the spheromak with the z' -axis aligned to the negative z-axis of the HEEQ system. This means that the main flow direction of the spheromaks magnetic field points southward. This indeed lead to a large and prolonged southward magnetic field component between 50 h and 74 h. The minimal Dst reached was -63.68 nT, classifying it as a moderate geomagnetic storm.

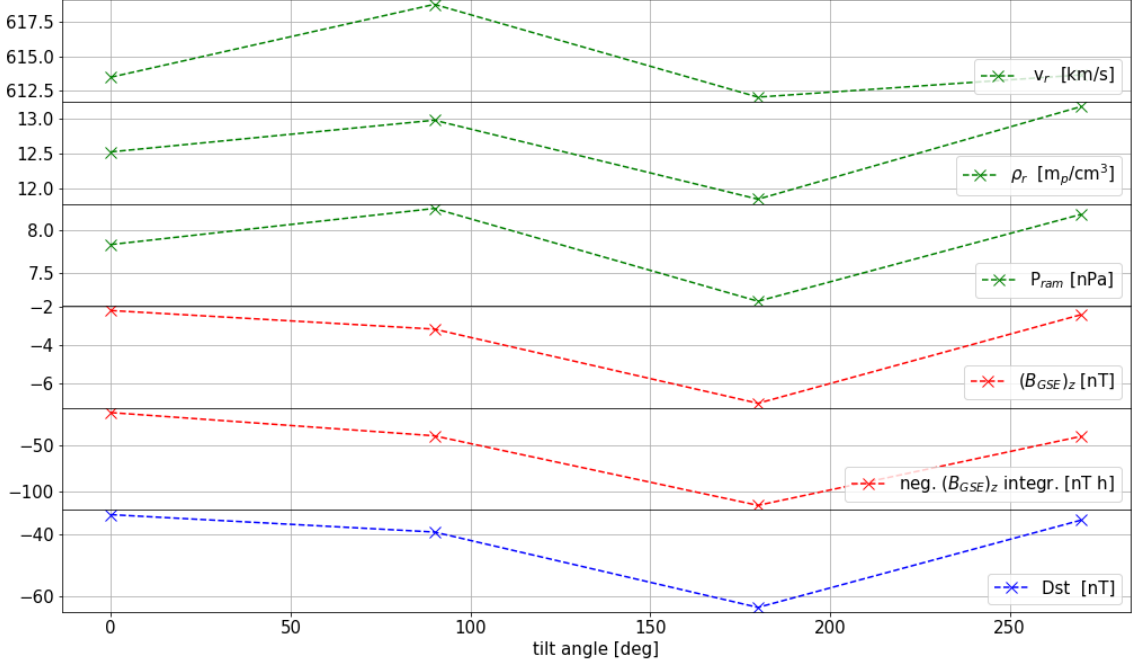


Figure 17: Maximal values of selected physical variables and integrated negative $(B_{GSE})_z$ for different tilt angles of CME0. The first three rows show plasma dynamical variables and the last three show the southward magnetic field, maximal and integrated and the minimal Dst.

The $\tau = 270^\circ$ run shows the same, but inverted features of the $\tau = 90^\circ$ run, as one would expect. The event would again lead to a weak geomagnetic storm as the minimal Dst was -35.23 nT.

This series of runs showed that the main direction of the magnetic field along the z' -axis does mostly survive out to 1 AU. The magnetic field in the y_{GSE} direction is hard to identify. It is very well possible that the magnetic field of the Parker spiral causes a distortion here. This can also be observed in the profiles from the $\tau = 180^\circ$ run in Figure 11. Here a significant deviation of the spheromaks magnetic cloud centre from the x-axis can be seen. This twist to the negative ϕ -direction in the HEEQ coordinates would be coherent with the negative B_ϕ component of the Parker spiral.

A summary of these simulation runs can be found in Figure 17. Besides selected plasma dynamical variables, the negative integrated $(B_{GSE})_z$ component is shown as a measure of how long the southward magnetic field component lasts in an event. Its trend is in line with the maxima of $(B_{GSE})_z$ itself. All variables shown in the figure indicate that a tilt angle of $\tau = 180^\circ$ leads to the largest geoeffectiveness. Therefore, this stage of the parametric study concluded that a significantly larger geoeffectiveness can be observed for a $\tau = 180^\circ$ tilt angle orientation for single CME events with respect to other orientations. Consequently, $\tau = 180^\circ$ was chosen for all consecutive runs.

3.5 Stage 2: Waiting Time

The second stage of the parametric study proceeded to investigate the interaction of two CMEs depending on the time between their respective insertion into the simulation domain. The second CME is initialized with a much higher total velocity of 1723 km/s compared to the first CME with 723 km/s and is thus gaining quickly on the first CME, see Table 3. The waiting time was varied from 12-36 h. This range encompasses the two boundary cases of 1) a collision at ~ 0.5 AU and 2) a pure preconditioning of the solar wind by the first CME. To judge the point at which a collision between the two CMEs occurs, is not trivial as some physical variables lead (e.g. ρ , v_r) and others lag (in particular B) in the propagation of CMEs. Here a collision of the density centres of the CMEs is dubbed as a collision of the CMEs, unless otherwise specified. The focus of this study is on the collision/interaction of the CMEs, as prior studies have already quantified the effect of preconditioning *Desai et al. (2020)* [6] for a real event.

All spheromaks were set to have a tilt angle of $\tau = 180^\circ$, expecting this would lead to the highest geoeffectiveness even in CME-CME interactions. Further, all spheromaks are set to have handedness $H = +1$.

A total of 7 simulations (plus CME0 and CME1 individually, so total 21 simulations) have been run leading to a waiting time resolution of 4 h. Separate simulations for CME0 and CME1 individually are run with the CMEs being inserted at their respective insertion times, just as in the CME0-CME1 run. This allows to compare the enhancement of the interaction CME0-CME1 to CME1 or CME0. The boundary cases and a very geoeffective case corresponding to a merger at 0.9 AU are discussed in detail in the following:

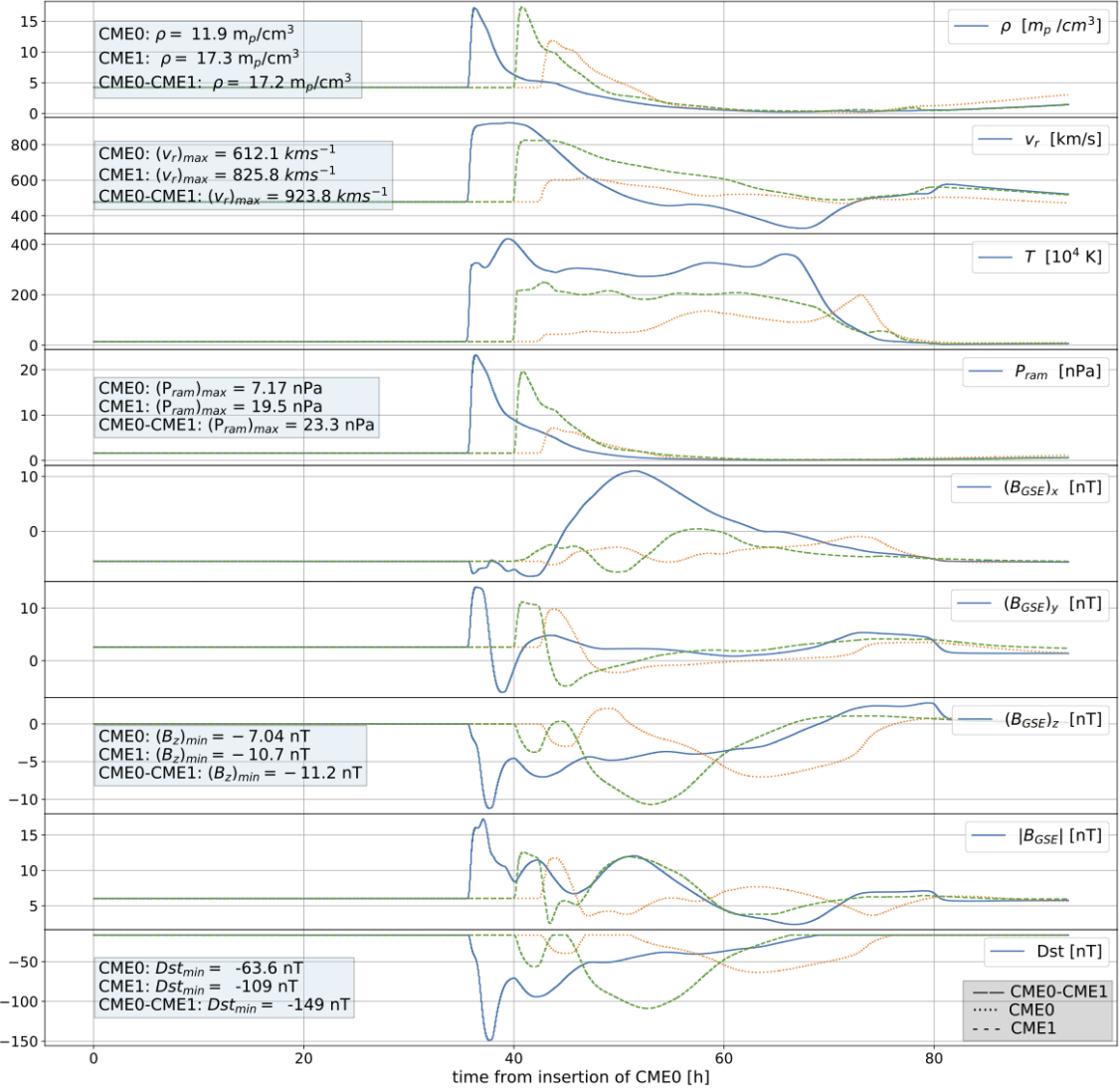


Figure 18: Virtual spacecraft data at 1 AU for the CME0-CME1 interaction of a waiting time of 12 h, corresponds to a merger of the density centres of the CMEs at approximately 0.5 AU.

12 h waiting time - This CME-CME interaction corresponds to a merger of the density centres of the CMEs at approximately 0.5 AU. The corresponding virtual spacecraft timeseries can be found in Figure 18, with dotted and dashed lines showing the CME0 and CME1 run individually.

The timeseries still shows all of the signatures of interplanetary CMEs, listed in Table 10, and thus can be said to represent a realistic CME-CME signature. The most striking feature of the timeseries is that all physical variables show an earlier commencement of the shock and flux rope in the CME0-CME1 case than in both individual runs CME1 and even CME0. This must be due to a preconditioning of the solar wind of the CME0 or/and the increase total momentum of the CME-CME ejecta. In either case, the drag forces of the solar wind are overcome such that the ejecta arrive quicker.

The initial shock can be identified as the region between 37-41 h followed by the CME-CME signature up to ~ 80 h. The shock is most apparent through the jump

in density, velocity and resulting dynamic pressure. Whilst little enhancement is found in the density jump in the CME0-CME1 timeseries compared to CME1, an enhancement of 11% can be seen in the peak velocity. Within the shock the magnetic field components show a high variance as expected.

The actual CME-CME signature (from 41 h onward) shows a strong depression in density and steep decline in velocity. The velocity even falls below the background solar wind speed and reaches a minimum of 281.90 km/s. The magnetic field components of the CME0-CME1 signature are completely different to the signatures of CME0 and CME1 individually. Especially $(B_{GSE})_x$ exhibits a very large component not seen in the individual CME signatures. This is probably due to some compression/rotation of the magnetic fields in the interaction. The signatures of CME0 and CME1 in $(B_{GSE})_y$ and $(B_{GSE})_z$ on the other hand seem to even each other out. There is a prolonged negative $(B_{GSE})_z$ component with a minimum of -11.2 nT, which represents only a slight enhancement compared to CME1. Nevertheless, a strong enhancement of 37% in Dst can be seen. The minimum achieved is -147 nT. This event corresponds to a severe geomagnetic storm. Note that the minimal Dst is found to be in a sheath region, where the relationship, used to calculate Dst, has large uncertainties, hence should be considered with care.

20 h waiting time - This situation resulted in a merger of the density centres of the CMEs at ~ 0.9 AU. A timeseries of the z-plane profiles can be seen in Figure 20. The interaction results in the CME0-CME1 shock arriving at the time the CME0 shock normally would have. The shock, or more precisely shocks, can be identified to be between 44 h and 50 h, followed by the CME signature up to 75 h. The density, velocity, temperature show a clear double step structure withing the shock. This is probably due to the shock fronts of CME0 and CME1 not yet being entirely, merged as the merger happened just 0.1 AU from Earth. Remarkable is the large enhancement of the density of 98% from 17.8 to $34.8 \text{ m}_p/\text{cm}^3$ between CME1 and CME0-CME1 respectively. The velocity shows the double step structure the most clearly, featuring a 41% increase to CME1. As in all prior simulations, the magnetic field exhibits an expected high variability within the shock, with a double peak in the southward magnetic field.

The CME signature itself shows an extraordinary low density region with a minimum of $0.15 \text{ m}_p/\text{cm}^3$, due to the prolonged and very high velocity double shock. The magnetic field shows the expected decrease in variability, yet surprisingly no significant depression in $(B_{GSE})_z$ can be seen within the CME. This observation that two spheromaks of tilt angle $\tau = 180^\circ$, i.e. maximal southward magnetic field flux, do not necessarily result in a strong depression of $(B_{GSE})_z$ within their CME signature when interacting is remarkable.

The minimal Dst thus comes from the double shock in front of the CME signature with the first peak reaching -267 nT, an 137% increase in geoeffectivness with respect to CME1 alone. This event would be classified as a severe storm.

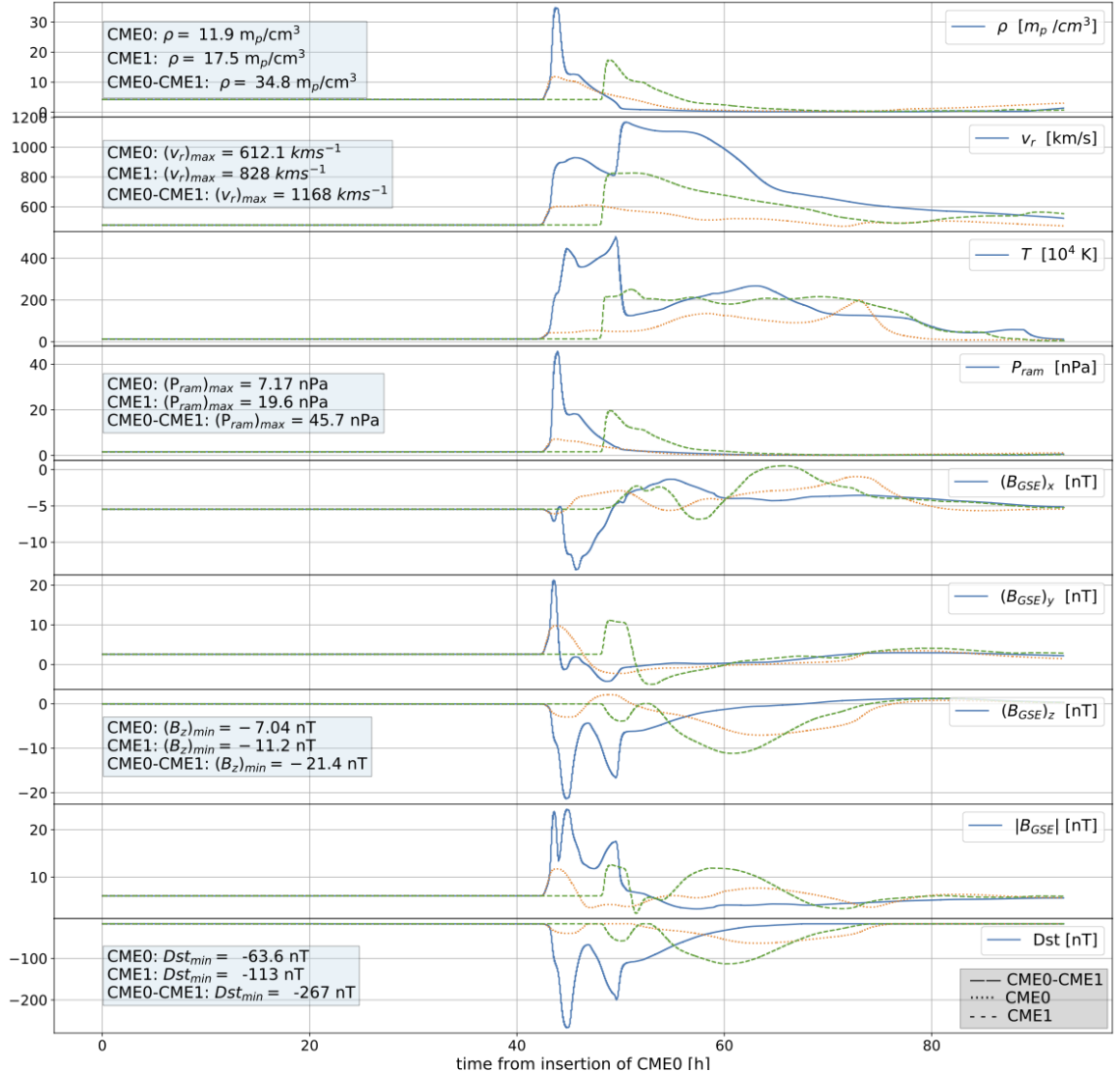


Figure 19: Virtual spacecraft data at 1 AU for the CME0-CME1 interaction of a waiting time of 20 h, corresponds to a merger of the density centres of the CMEs at approximately 0.9 AU.

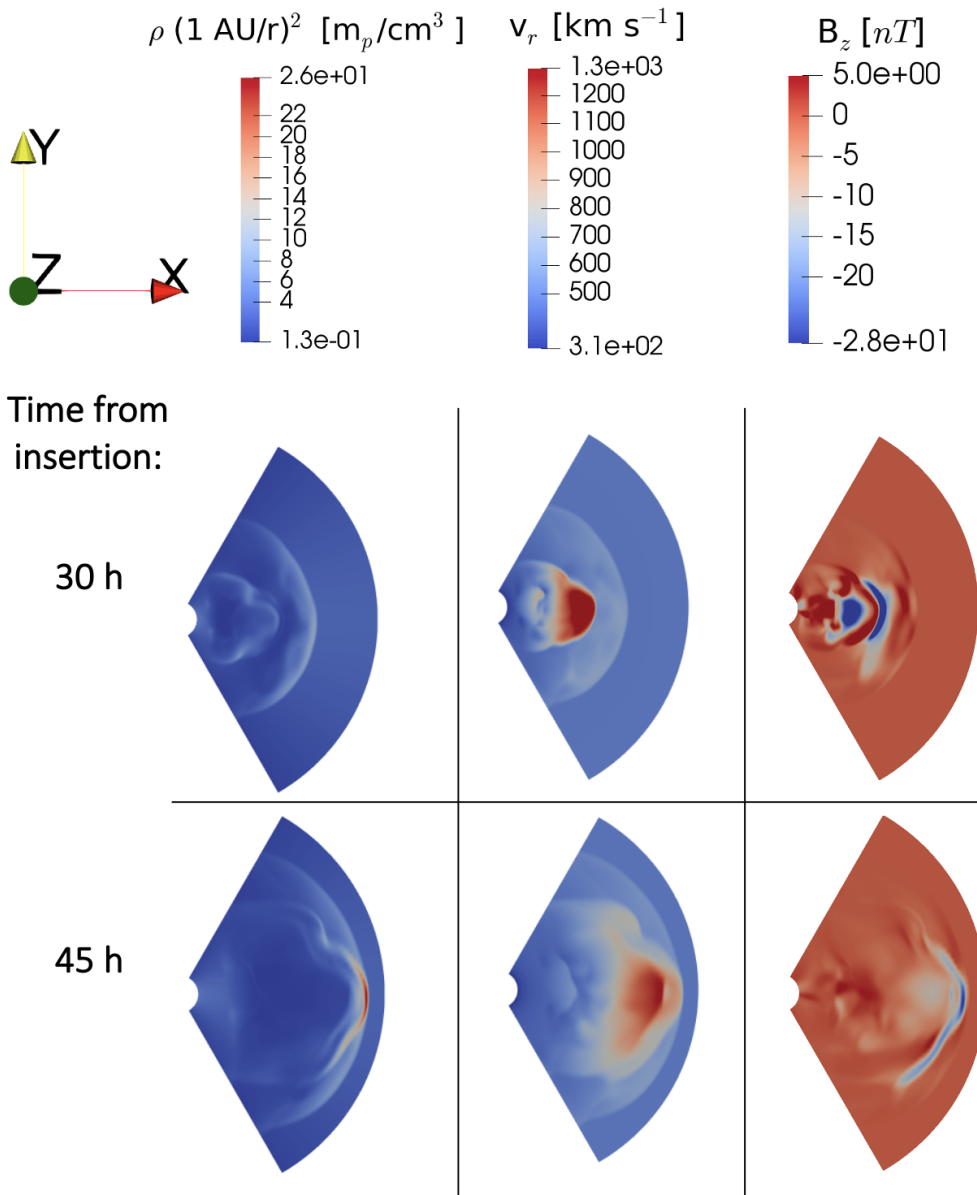


Figure 20: Timeseries of z-plane profiles of normalized density (left), radial velocity in HEEQ system (middle) and $(B_{GSE})_z$ component for the collision of CME0 and CME1 with a waiting time of 20 h. Note the deviation from the x-axis due to the Parker spiral in the 45 h row.

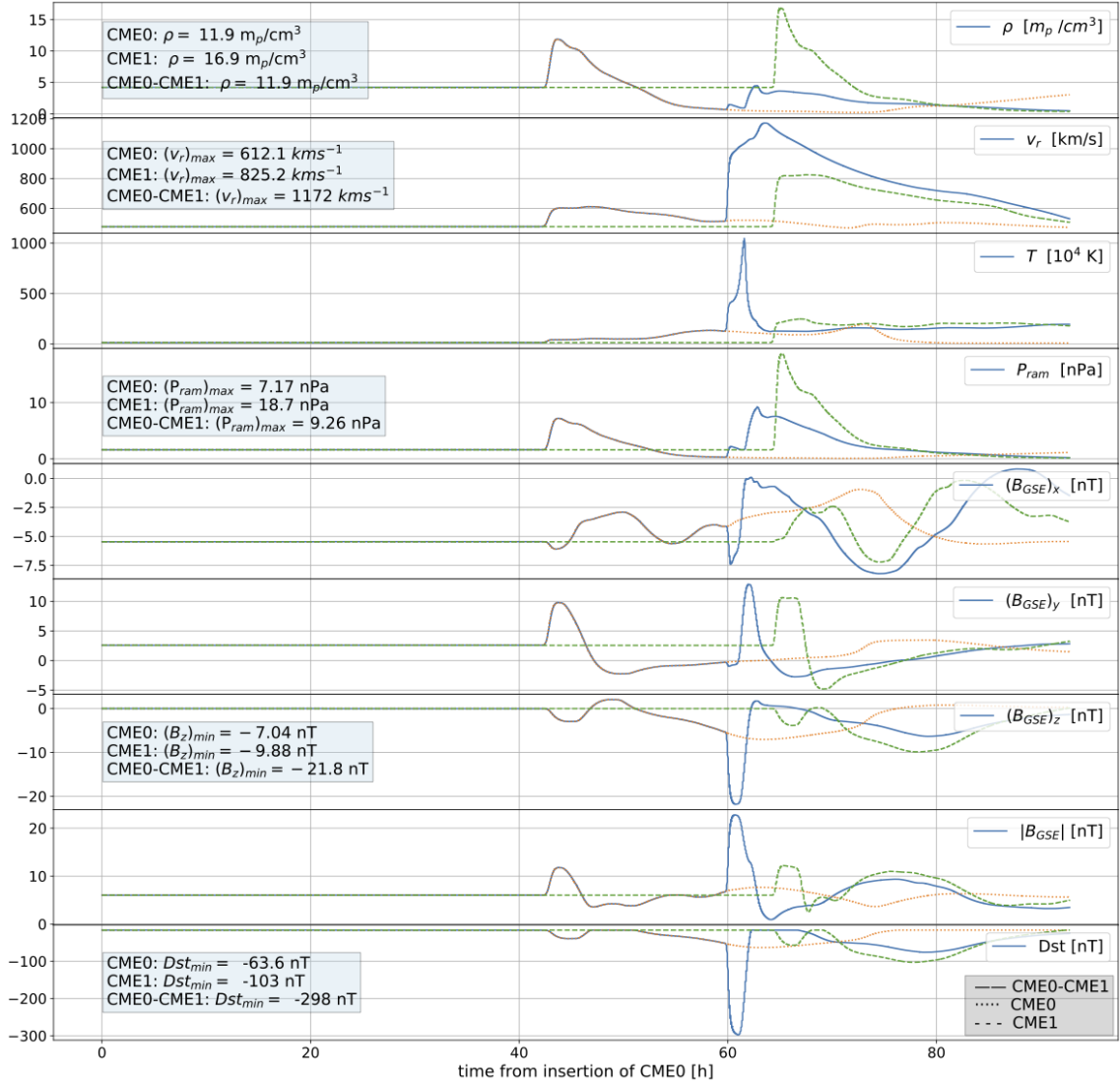


Figure 21: Virtual spacecraft data at 1 AU for the CME0-CME1 interaction of a waiting time of 36 h, corresponds to a pure preconditioning case - no hit of the density centres within the simulation domain.

36 h waiting time - This CME-CME situation simulated a case in which little direct interaction between CME0 and CME1 is observed. Their interaction is mostly mediated due to a preconditioning of the solar wind. The CME0-CME1 signature shows the undisturbed CME0 signature from 43 h to 57 h followed by the shock of CME1 up to 68 h and the actual CME flux rope signature after.

A remarkable feature of the second shock due to CME1 is the very low density spike of below $5 \text{ m}_p/\text{cm}^3$, yet a very high velocity of 1172 km/s leading to a very low maximal dynamic pressure of 9.26 nPa compared to 18.7 nPa for CME1 alone. The southward magnetic field only shows a significant depression in the second shock. The minimal Dst is -298 nT, representing a 198% increase to CME1. This event would be classified as a very severe geomagnetic storm.

Summary of Waiting Time Runs - To draw conclusions about the relationship between geoeffectivness and waiting time the absolute maxima in CME0-CME1 and deltas of the maxima between CME0-CME1 and CME1 were collected for selected physical variables. The results are summarised in Figure 23 and Figure 22. The virtual spacecraft timeseries of all other runs can be found in Appendix E.

The range of waiting times captures both mergers in the inner heliosphere and pre-conditioning cases. Waiting times of 12 h, 16 h, 20 h and 24 h correspond to mergers of the density centres at ~ 0.5 AU, 0.7 AU, 0.9 AU and just after Earth respectively. All other runs don't exhibit a merger within the simulation domain, extending up to 1.1 AU. Thus one may identify the first three data points, 12-20 h, as pure merger events and the last two, 32-26 h , as mostly preconditioning cases. The events in the middle show features of both regimes.

The maximal and delta velocity show a plateau of a maximal velocity of approximately 1200 km/s and a relative increase between CME1 and CME0-CME1 of 400 km/s. Short waiting times don't seem to allow sufficient time for propagation of the CME0 to have an impact on the speed of propagation of CME1. The 36 h waiting time case already shows a recovery of the solar wind speed to its normal state.

The maximal and delta density show an increase up to the 20 h waiting time case and a depression after. This depression has been explained in detail for the 36 h case earlier.

These velocity and density profile lead to a maximum in dynamic pressure at a waiting time of ~ 20 h for this CME-CME situation.

The southward magnetic field component shows a smooth depression with a bottom around 28 h. As mentioned earlier, the magnetic field appears to consistently lag behind the density and velocity propagation. Thus, the 28 h case does correspond to an actual collision of magnetic signatures of the CMEs around Earth, even though the density centres miss each other. Also here a recovery to the solar wind normal can be seen for long waiting times.

The Dst reaches its minimum close to the 28 h case, with a Dst of -401 nT, which would result in a classification as an extreme/great event. It must be emphasised here that the Dst relationship used, is only linear in velocity and is not a good predictor for high velocity events as investigated here. Further, all Dst extrema were found to be in sheath/shock regions were the relationship has large uncertainties. [51] Nevertheless, the consensus of these physical variables suggest that the case of maximal geoeffectivness is within the range of 20-28 h waiting time.

All statements made here are only applicable to this very situation in terms of velocity, initial size and magnetic strength of two interacting CMEs. Nevertheless, it provides a useful intuition about CME-CME interactions in general.

All consecutive runs used a waiting time of 20 h, as this represents a geoeffective merger of density centres at 0.9 AU. This case is investigated a lot in the space physics community, as it is thought to lead to the most severe events.

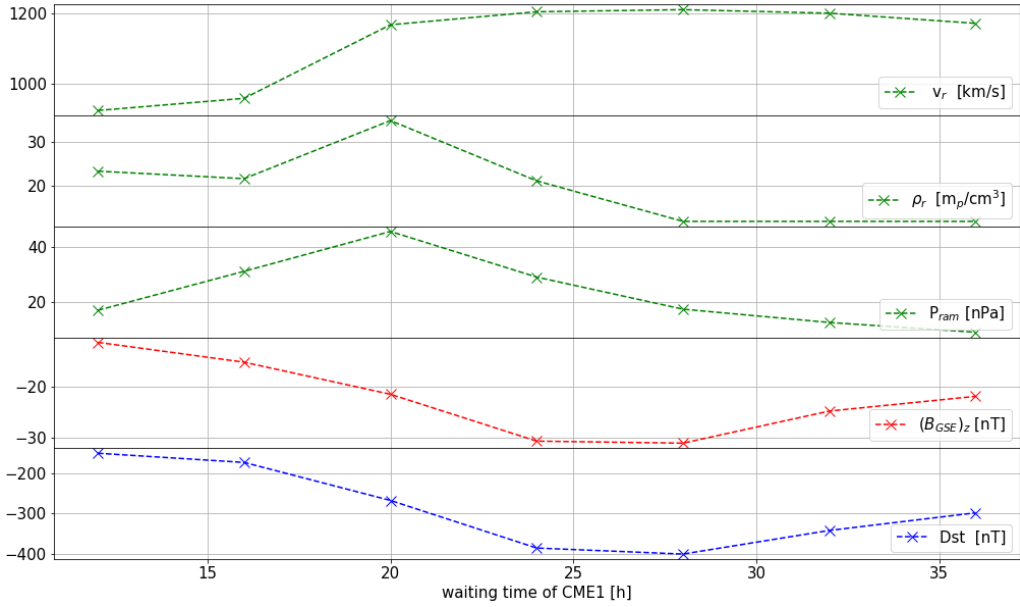


Figure 22: Maximal values of selected physical variables related to geoeffectiveness for different waiting times between CME0 and CME1. The first three rows show plasma dynamical variables and the last two show the southward magnetic field and the Dst.

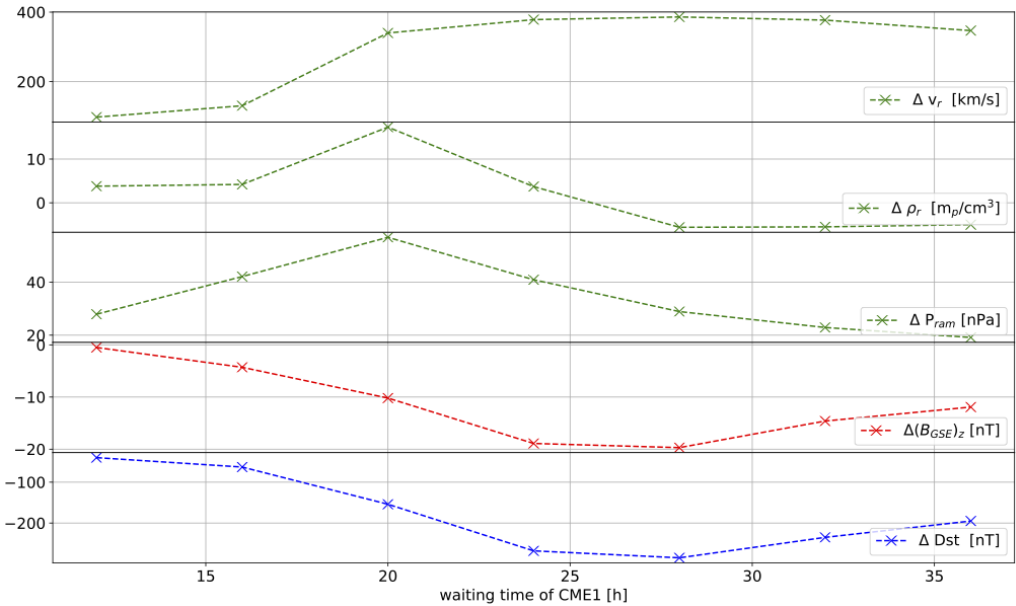


Figure 23: Deltas of maxima of selected physical variables related to geoeffectiveness for different waiting times between CME0 and CME1. The delta is calculated between the CME0-CME1 and CME1 events. The rows correspond to Figure 22.

3.6 Stage 3: Handedness

The third and last stage of this parametric study concerned itself with the handedness H . The handedness defines the sign of the B'_ϕ component, see Equation 17. A positive handedness $H = +1$ results in the magnetic field lines turning counter-clockwise looking down on the spheromak from the positive z' -plane. A negative handedness correspondingly results in a clockwise rotation in the B_ϕ component. The intention of this stage was to test whether a particular handedness combination would result a more geoeffective interaction, due to magnetic reconnection or other effects. It must be emphasized that the initial $(B_{GSE})_z$ component of the spheromak is not altered, thus only a rotation or translation of the magnetic structure can result in a different magnetic signature at 1 AU. A total of four simulation runs have been made to capture all combinations of $H_0 = \pm 1$ and $H_1 = \pm 1$. In the following we shall refer to each run as $H:[H_0, H_1] = H:[\pm 1, \pm 1]$.

Figure 24 shows a timeseries of z-plane profiles of the $(B_{GSE})_z$ component of the magnetic field for all combinations of H . At first sight these profiles look very similar, as one would expect, yet there are subtle, but significant differences. The first row shows the profiles for 21 h after the insertion of CME0 and just 1 h after the insertion of CME1. The spherical shape of CME1's spheromak is still clearly visible. CME0 already propagated outward forming a positive shock in $(B_{GSE})_z$. Particular focus should be put on the shape of the large negative region of CME0. For a positive handedness the shape of the negative area becomes thinner with in negative y -direction. The opposite can be seen for negative handedness.

The next row, 30 h, shows the compression of the opposite polarity magnetic field areas with various differences. These difference lead to a significant drift of the elongated negative region in timestep 40 h. Here the elongated negative region is just about to hit Earth. A clear trend can be identified. A positive H leads to a drift in the clockwise direction and vice versa. In the consecutive propagation, in the 50 h timestep, the differences become clearer.

From this is not obvious how these differences emerge due to a variation of the handedness of the spheromaks.

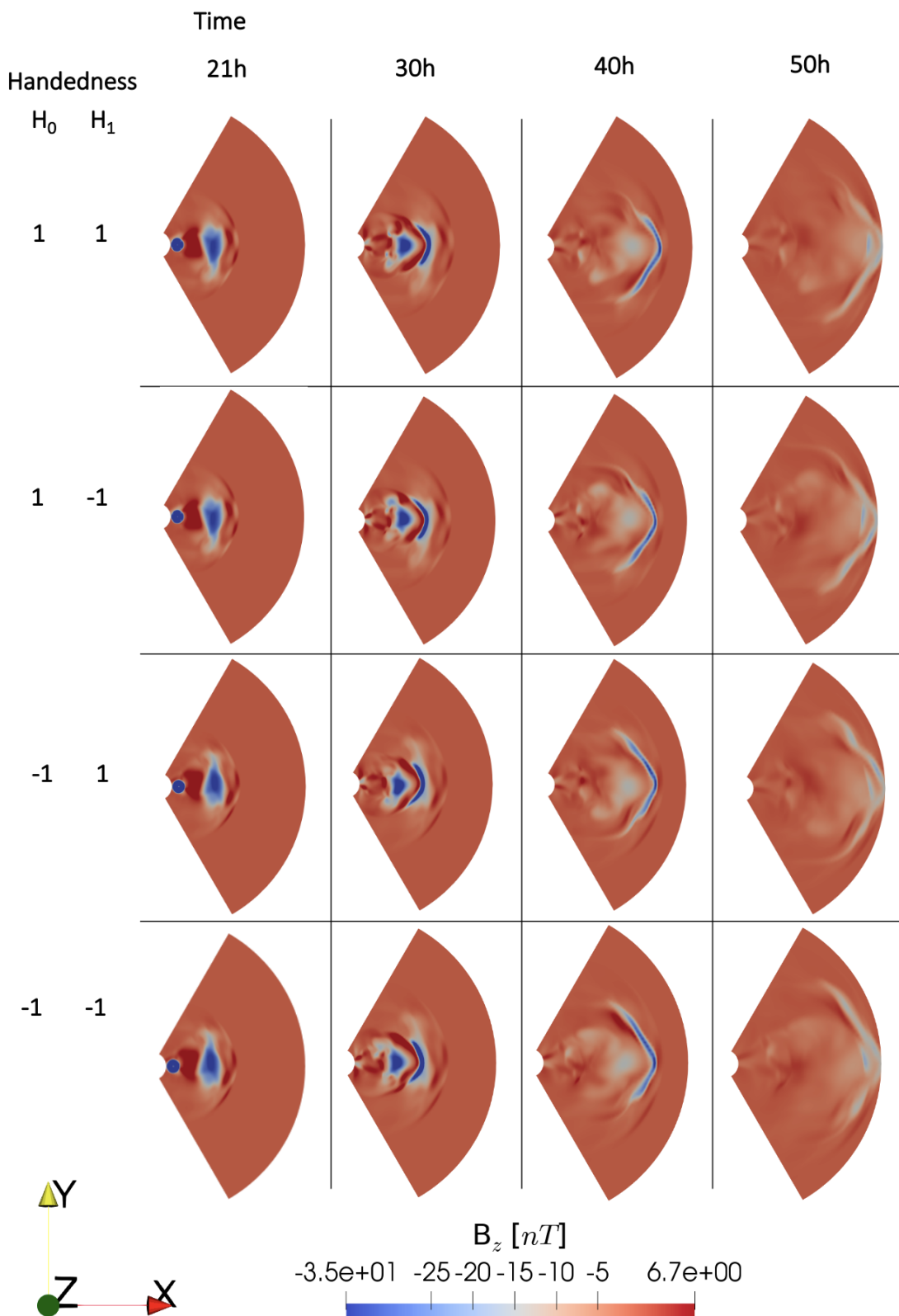


Figure 24: Timeseries of z-plane profiles of $(B_{GSE})_z$ for the collision of CME0 and CME1 for different handedness with a waiting time of 20 h and tilt angles of $\tau = 180^\circ$.

Handedness		Max/Min values			
H_0	H_1	$(\rho)_{max}$ [m _p /cm ³]	$(v_r)_{max}$ [km/s]	$((B_{GSE})_z)_{min}$ [nT]	$(Dst)_{min}$ [nT]
1	1	33.7	1144	-21.8	-275
1	-1	33.0	1166	-20.1	-243
-1	1	34.4	1132	-17.6	-212
-1	-1	32.4	1180	-12.7	-163

Figure 25: Summary of maximal values of handedness runs.

For completeness, a timeseries of the virtual spacecraft data of the space weather conditions at Earth is shown in Figure 26 for the H:[-1, -1] case and the rest of the runs can be found in the Appendix F. If one compares the H:[-1,-1] case to the H:[+1, +1] case, shown earlier in Figure 19, a few clear changes are visible. These features include a single large peak in temperature compared to two smaller ones and a higher variation in the magnetic field components. The resulting Dst shows a reduced depression, leading to a lower geoeffectivness.

The difference between the runs is more apparent in tabular form of the maximal values, see Table 25. Even though all runs are initialized with the same $(B_{GSE})_z$ structure, a large variation in the signatures at Earth is found. A clear trend from positive to negative handedness can be identified. Note that the handedness of the first CME seems to have a higher influence than the handedness of the second CME. The maximal the southward magnetic field varies between -12.7 to 21.8 nT. This is a 71% difference. The dynamic variables show no significant trend. The resulting Dst shows the same trend as the magnetic field from -163 to -275 nT, a 68% change. Note again that maxima in Dst are found in sheath/shock regions.

These difference in geoeffectivness would already change the classification of the geomagnetic storm from strong to severe. It is a major finding that the handedness of spheromak in CME-CME interactions can have such a dramatic effect of the geoeffectivness.

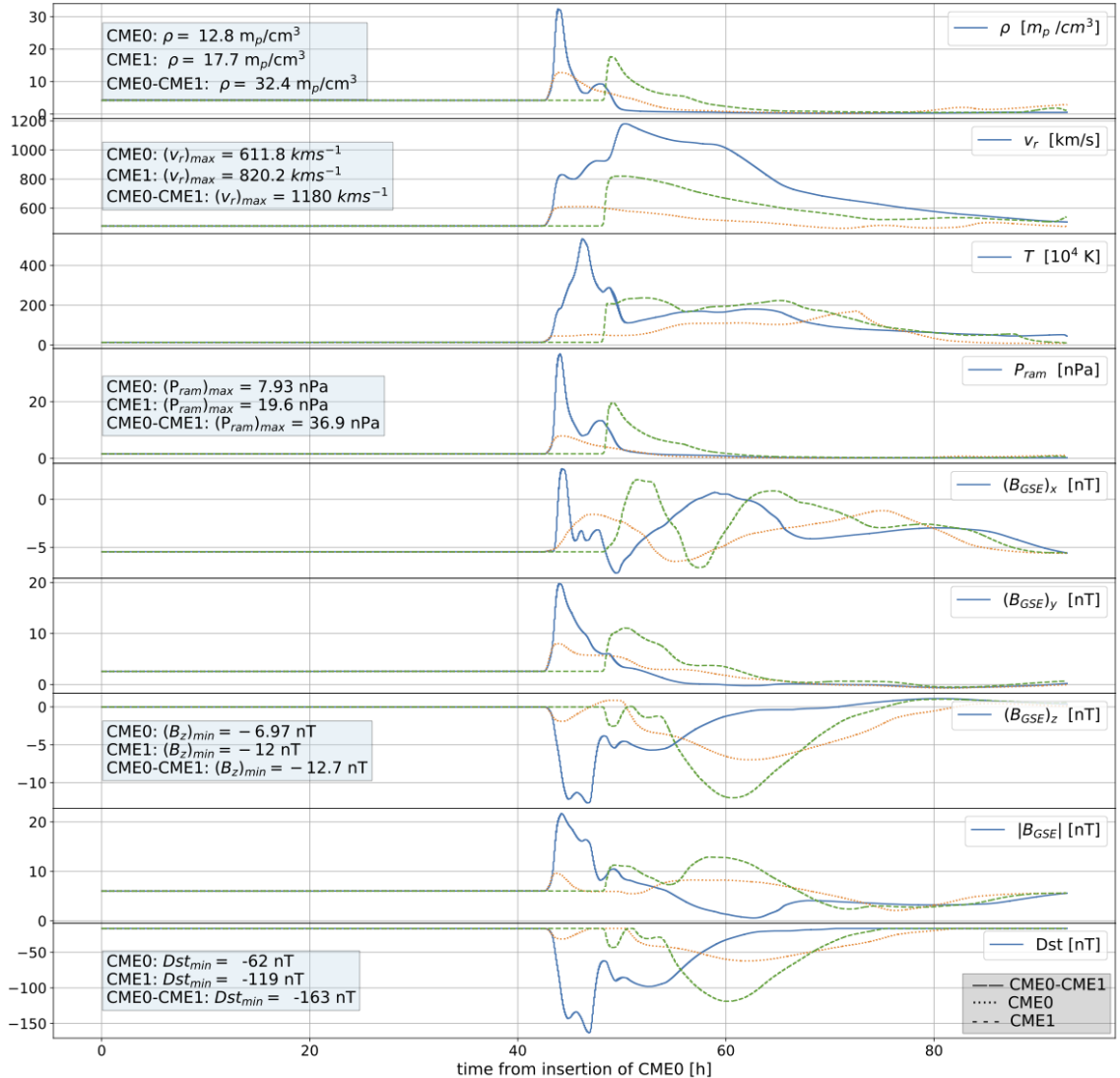


Figure 26: Virtual spacecraft timeseries at 1 AU for a CME0-CME1 interaction of handedness $H_0 = -1$, $H_1 = -1$. (waiting time 20 h, both tilt angles $\tau = 180^\circ$)

To investigate the cause of this dramatic impact, Figure 27 shows the y -plane profiles of B_ϕ and the 3D magnetic flow lines projected onto that plane. It only includes the most and least geoeffective cases, $H:[+1,+1]$ and $H:[-1,-1]$ respectively. This figure indicates the possible cause for this dramatic difference in geoeffectiveness. The $H:[+1,+1]$ case exhibits a winding of magnetic field lines in the CME-CME region in comparison to the $H:[-1,-1]$. This is most clearly visible in timestep 30 h. This behaviour may be explained as follows. For a spheromak of $\tau = 180^\circ$ a handedness of $H = +1$ means that the internal magnetic field lines in the toroidal direction flow in the same sense as the Parker spiral on the radially outward propagating side. This allows the winding of field lines within the spheromak to survive longer. This winding or toroidal flow gives stability to the magnetic ejecta leading to a prolonged compression of field lines. A negative handedness, $H = -1$, on the other hand leads to field lines of spheromak and Parker spiral flowing into opposing directions on the outward radial side. This may explain the de-facto dispersion of magnetic density for the $H:[-1,-1]$ case.

The above explanation would be supported by the observation that the first CME's handedness seems to have a larger effect than that of the second one, see the progressive trend in Table 25. This is because only the first CME strongly interacts with the Parker spiral, whereas the second CME travels within the preconditioned/disturbed solar wind.

The discovery that the handedness of spheromaks, representing interplanetary CMEs, dramatically influences the geoeffectiveness of CME-CME events, is the major novel finding of this report. The proposed mechanism of winding field lines, as the possible cause of the enhancement of the geoeffectiveness, needs further investigation.

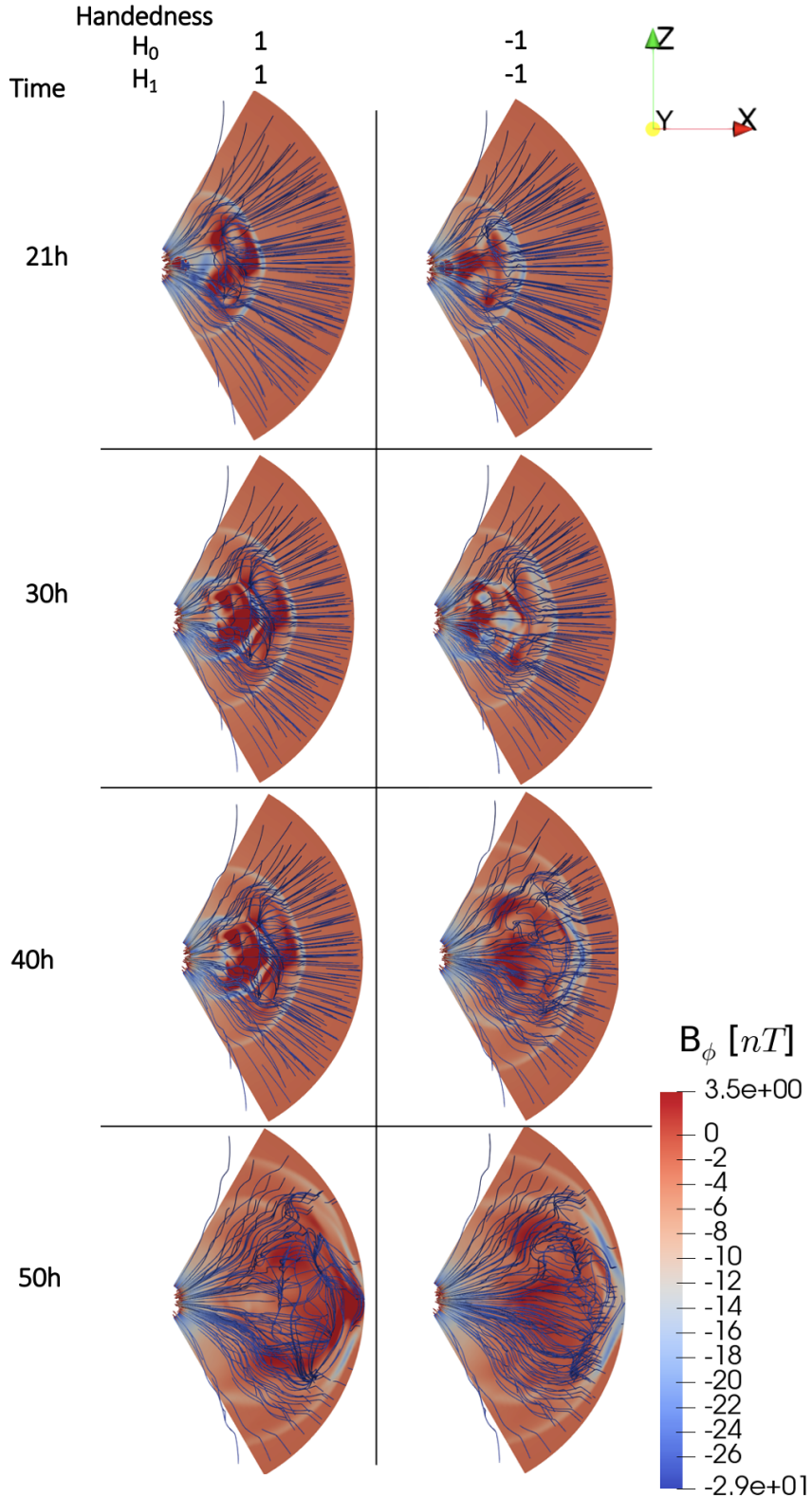


Figure 27: Timeseries of y-plane profiles and 3D magnetic field lines of (B_ϕ) for the collision of CME0 and CME1 for different handedness (most and least geoeffective) with a waiting time of 20 h and tilt angles of $\tau = 180^\circ$. The interaction of the handedness of the CMEs and the Parker spiral can be seen here. Note that the field line tracing may be subject to inaccuracies and sampling issues, and hence may miss important features.

4 Discussion & Conclusion

This study successfully conducted a parametric study of coronal mass ejection interactions in a representative heliospheric environment employing the novel linear force-free spheromak model using the PLUTO MHD code. The model has been verified to reproduce the typical morphology and spacecraft timeseries signatures of interplanetary coronal mass ejections. Further, the existence of a flux rope at 1 AU was proven by a minimal variance analysis. This is despite the restriction the PLUTO environment placed on the method of initializing of the spheromak, representing a coronal mass ejection. The spheromak had to be inserted instead of injected as commonly done.

The parametric study investigated the impact of the variation of the tilt angle for single CMEs and the impact of waiting time and handedness for CME-CME interactions. The findings are summarised in the stages of the parametric study below:

Single CME - Tilt angle

- The major magnetic field direction of the spheromak at 0.1 AU has a direct impact on its geoeffectiveness. A tilt angle of $\tau = 180^\circ$ showed the minimal B_z component at Earth.
- Single coronal mass ejections simulated with the spheromak model can lead to full magnetic cloud signatures at Earth, in comparison to earlier CME models.

CME-CME - Waiting Time

- The interaction of spheromak CMEs (even of identical structure) can result in magnetic signatures completely unlike their individual ones.
- Large southward magnetic field values can emerge due to the compression between two CMEs.
- CME-CME situations of long waiting times can experience an enhancement of geoeffectiveness due to a preconditioning of the solar wind, verifying the findings from *Desai et al. (2020)* [6].
- The particular situation of a slow and fast CME simulated here, experiences a distinct behaviour with respect to the waiting time. The maximal dynamic pressure consistently occurs for shorter waiting times than the minimal southward magnetic field (B_{GSE}) $_z$, see Figure 23.
- A merger of two CMEs just before Earth (~ 0.9 AU) of the density (magnetic) centres leads to the maximal impact on plasma dynamical (magnetic) variables in space weather conditions at Earth.

CME-CME - Handedness

- The handedness between CMEs was shown to have a surprisingly large effect on the southward magnetic field signature at Earth. In the particular situation modeled here a 71% increase was measured.
- An interaction of a spheromaks handedness and the interplanetary magnetic field due to the Parker spiral may cause a prolonged conservation of toroidal flux, leading to an increase in southward magnetic field strength at Earth.

These findings allow for a better understanding how CMEs can enhance each other to create a *perfect storm*, as termed by, *Liu (2014)* [5], of 'Carrington' scale. This study suggests that a perfect storm would have the following characteristics:

A merger of two CMEs with the major magnetic field direction into the southward direction (spheromaks of $\tau = 180^\circ$) and with a waiting time between the successive eruptions such that the density/magnetic centres (depending on the definition of geoeffectiveness) hit just in front of Earth (~ 0.9 AU). Further, both CMEs should be of a handedness such that the spheromak's toroidal flux is in the same sense as the Parker spiral on its radially outward propagating side. ($H = +1$)

The major novel finding of this project is that handedness of the spheromaks representing interplanetary coronal mass ejections in CME-CME events does dramatically influence the geoeffectiveness of the event. The cause of this should be investigated more thoroughly.

In further works, an advanced inner radial boundary should be implemented to inject the spheromak through the inner boundary instead of inserting it, as commonly done for a more realistic initialization of the CME. To quantify the actual geoeffectiveness in terms of Dst, a more applicable relationship than the one used here from *Wu et al. (2005)* [51] should be selected. With these improvements a deeper parametric study should be conducted, without any a priori discrimination against some tilt angles. A certain tilt angle may lead to a weak geoeffectiveness in single CME events, but may prove to cause to a disproportionately higher geoeffectiveness in CME interactions.

For simulations of real events, with spheromak injection, dynamic heliospheric conditions should be implemented.

It takes about 55 min of computation to simulate a CME propagation to 1 AU, on a typical resolution of $0.788 R_s$ radially and 2° angular using 48 CPUs. With this robustness and relatively low computational requirements, this model could be used as an operational tool for space weather prediction.

Acknowledgements

The author of this paper would like to thank the following people for their contribution to this project:

Dr. Ravindra Desai (Imperial College London) - for his caring supervision of the project.

Dr. Julia E. Stawarz (Imperial College London) - for her advice with the spheromak structure.

Dr. Emma Davies (University of New Hampshire) - for her advice with flux rope signatures and for performing a minimal variance analysis.

Imperial College Research Computing Service - for the means to conduct this highly computational study.

Declaration of Work

A thesis submitted in partial fulfilment of the requirements for the degree of Master of Physics and the Diploma of Imperial College London.

All work presented here is my own work, is not copied from any other person's work (published or unpublished) unless otherwise indicated.

Selected parts of this report were adapted from a literature review submitted under my name as part of this project.

Visualization in this report were created using the ParaView software and the matplotlib python libraries. Computations for this project were conducted on the High-Performance Computing (HPC) facilities of Imperial College London.

Appendices

Appendix A Spherical Bessel Function of Order One

The spherical Bessel function, $j_n(x)$, represents one of two linear independent solutions to the Helmholtz equation in spherical coordinates. Its first order solution $j_1(x)$ finds application in the LFFS model and is defined as

$$j_1(x) = \frac{\sin x}{x^2} - \frac{\cos x}{x}, \quad (21)$$

leading to the behaviour seen in Figure 28. The first zero is at $x \approx 4.4934094579$ and it used to set the radial extend of the spheromak in the LFFS model.

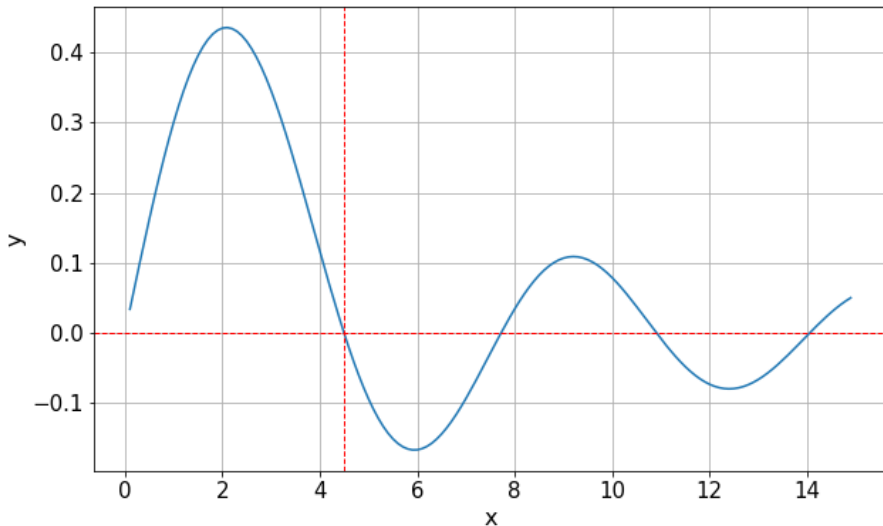


Figure 28: Spherical Bessel function of order one. The red lines indicate its first zero.

Appendix B From ϕ_t to Spheromak Parameters

In the main text a direct relationship between the total toroidal flux ϕ_t and the magnetic field strength scale parameter B_0 is mentioned. This purely geometric relationship is:

$$\phi_t = \frac{2B_0}{\alpha^2} \left(-\sin(\alpha r_0) + \int_0^{\alpha r} \frac{\sin x}{x} dx \right). \quad (22)$$

All variables have the same meaning as in the main text. The parameter B_0 can be found from the poloidal magnetic flux ϕ_p as

$$B_0 = \frac{\alpha^3}{2\pi} \frac{\phi_p(r_*)r_*}{(\sin(\alpha r_*) - \alpha r_* \cos(\alpha r_*))}, \quad (23)$$

where r_* is the distance from the centre of the spheromak, in the $\theta = \pi/2$ plane, in which the magnetic field becomes completely axial, only B_ϕ is non-zero.

The poloidal flux can be estimated from remote sensing observations. See *Scolini et al. (2019)* [13] for details and context.

Appendix C Coordinate Transformations and Vector Translations

A practical difficulty in the implementation of the LFFS model is to encode the local spherical spheromak structure in a global cartesian/spherical simulation grid. The process of translations and transformations used to encode the spheromak is explained here for ease of reconstruction and understanding of this project:

- 1) PLUTOs simulation grid was chosen to be 3D spherical (r, θ, ϕ) , defined as commonly used in physics in line with (ISO 80000-2:2019 convention). It reflects the HEEQ system.
- 2) The first step in shifting to the local spherical coordinate system of the spheromak (r', θ', ϕ') is to convert the spherical HEEQ coordinates to the cartesian HEEQ (x, y, z) coordinates, using:

$$\begin{cases} x = r \cos \phi \sin \theta \\ y = r \sin \phi \sin \theta \\ z = r \cos \theta \end{cases} \quad (24)$$

Then a 1D translation is performed on the spheromak's centre by subtraction on the x-coordinate. To arrive in the spheromak's local cartesian coordinates (x', y', z') , a 2D rotation is performed to implement the tilt angle of the spheromak as:

$$\begin{cases} y' = z \sin \tau_{CME} + y \cos \tau_{CME} \\ z' = z \cos \tau_{CME} - y \sin \tau_{CME} \end{cases} \quad (25)$$

- 3) As the spheromak is defined in spherical coordinates a last coordinate transformation, as in Equation 24, is applied to arrive in the local spherical coordinates (r', θ', ϕ') , in which its structure is defined.
- 4) In this frame the B' components of the spheromak are calculated. Note that the definition of the spheromak's B'_r component needs an additional minus in this coordinate definition. This is apparently due to an opposite definition of the radial unit vector in *Verbeck et al. (2019)* [12]. Here it points to the origin, not from it.
- 5) The local spherical magnetic field components are then converted to the local cartesian coordinates using the transformation matrix below:

$$\begin{pmatrix} B'_x \\ B'_y \\ B'_z \end{pmatrix} = \begin{pmatrix} \sin \theta' \cos \phi' & r' \cos \theta' \cos \phi' & -r' \sin \theta' \sin \phi' \\ \sin \theta' \sin \phi' & r' \cos \theta' \sin \phi' & r' \sin \theta' \cos \phi' \\ \cos \theta' & -r' \sin \theta' & 0 \end{pmatrix} \begin{pmatrix} B'_r \\ B'_\theta \\ B'_\phi \end{pmatrix} \quad (26)$$

- 6) Subsequently, a rotation is performed on these cartesian local cartesian vectors as a first step to move back to the global HEEQ coordinates. This is done by a 2D rotation to align z' and z-axis of HEEQ system by:

$$\begin{cases} B_y = B_z \sin(-\tau_{CME}) + B_y \cos(-\tau_{CME}) \\ B_z = B_z \cos(-\tau_{CME}) - B_y \sin(-\tau_{CME}) \end{cases} \quad (27)$$

7) The final step to the HEEQ spherical vectors of the magnetic field is mediated by another transformation matrix written as:

$$\begin{pmatrix} B_r \\ B_\theta \\ B_\phi \end{pmatrix} = \begin{pmatrix} \sin \theta \cos \phi & \sin \theta \sin \phi & \cos \theta \\ (\cos \theta \cos \phi)/r & (\cos \theta \sin \phi)/r & -\sin \theta/r \\ -\sin \phi/(r \sin \theta) & \cos \phi/(r \sin \theta) & 0 \end{pmatrix} \begin{pmatrix} B_x \\ B_y \\ B_z \end{pmatrix} \quad (28)$$

Appendix D Simulation Code

The simulation code of this project can be found online upon request or publicly available after academic review:

https://github.com/gordonkoehn/phaethon_CME-CME_LFFS_model

The code allows for easy modification of spheromak parameters and still includes the code for the injection of the spheromak.

For further instructions of usage see the *README* in the repository or contact the author of this report.

The computational units used in this simulation are placed here for ease of usage of this simulation, see Table 29.

Quantity	Factor	Unit
Density	20	m_p/cm^3
Pressure	33.452	nPa
Velocity	10^7	cm/s
Length	$R_S = 6.960 \cdot 10^{10}$	cm
Temperature	$1.203 \cdot 10^6$	K
Time	6690	s
Magnetic Field	20.5031	nT

Figure 29: PLUTO code computational units used for this project.

Appendix E Waiting Time Simulation Runs

Here the remaining virtual spacecraft timeseries of Stage 2 are presented for completeness:

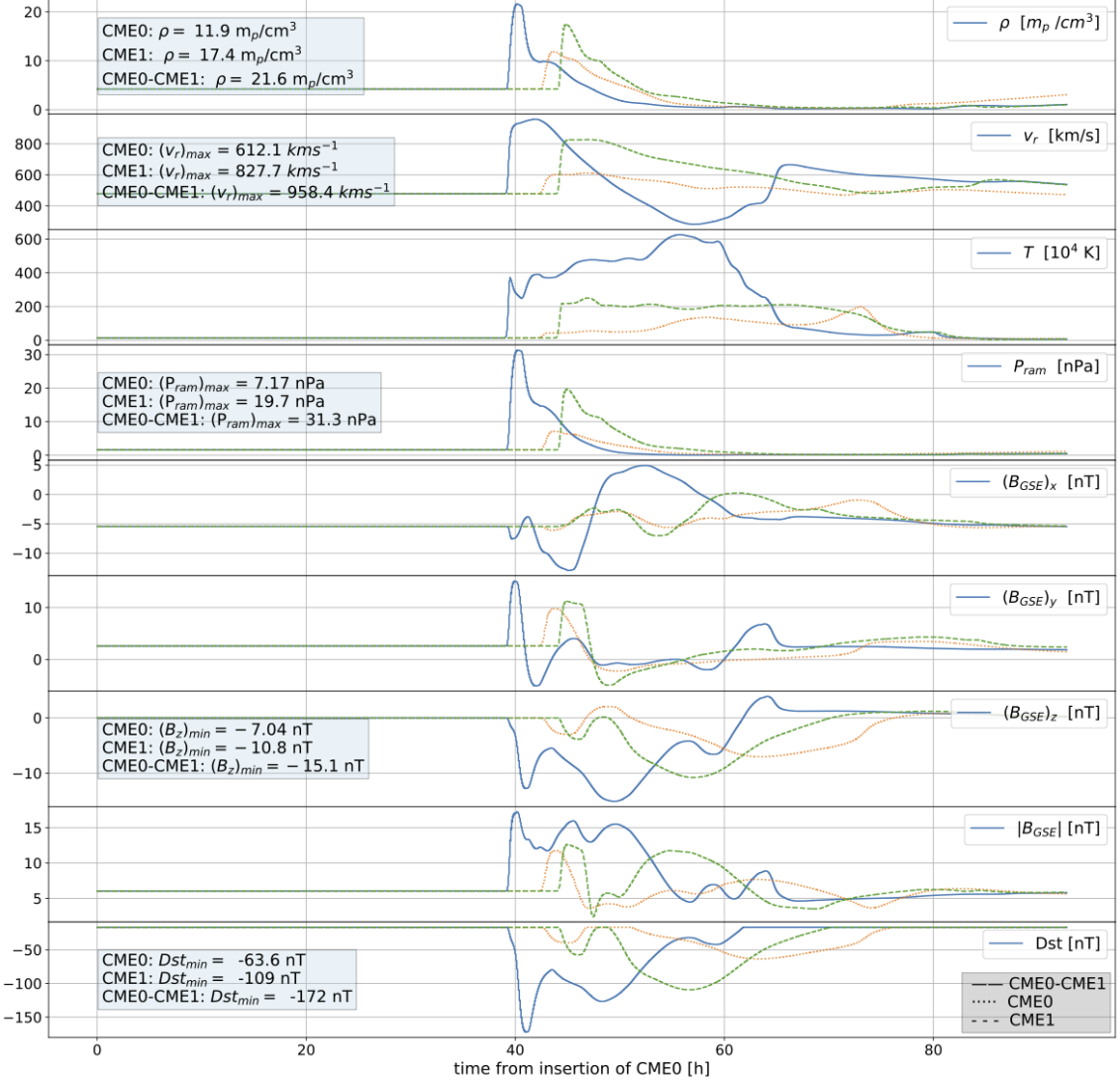


Figure 30: Virtual spacecraft data at 1 AU for a CME0-CME1 interaction of a waiting time of 26 h

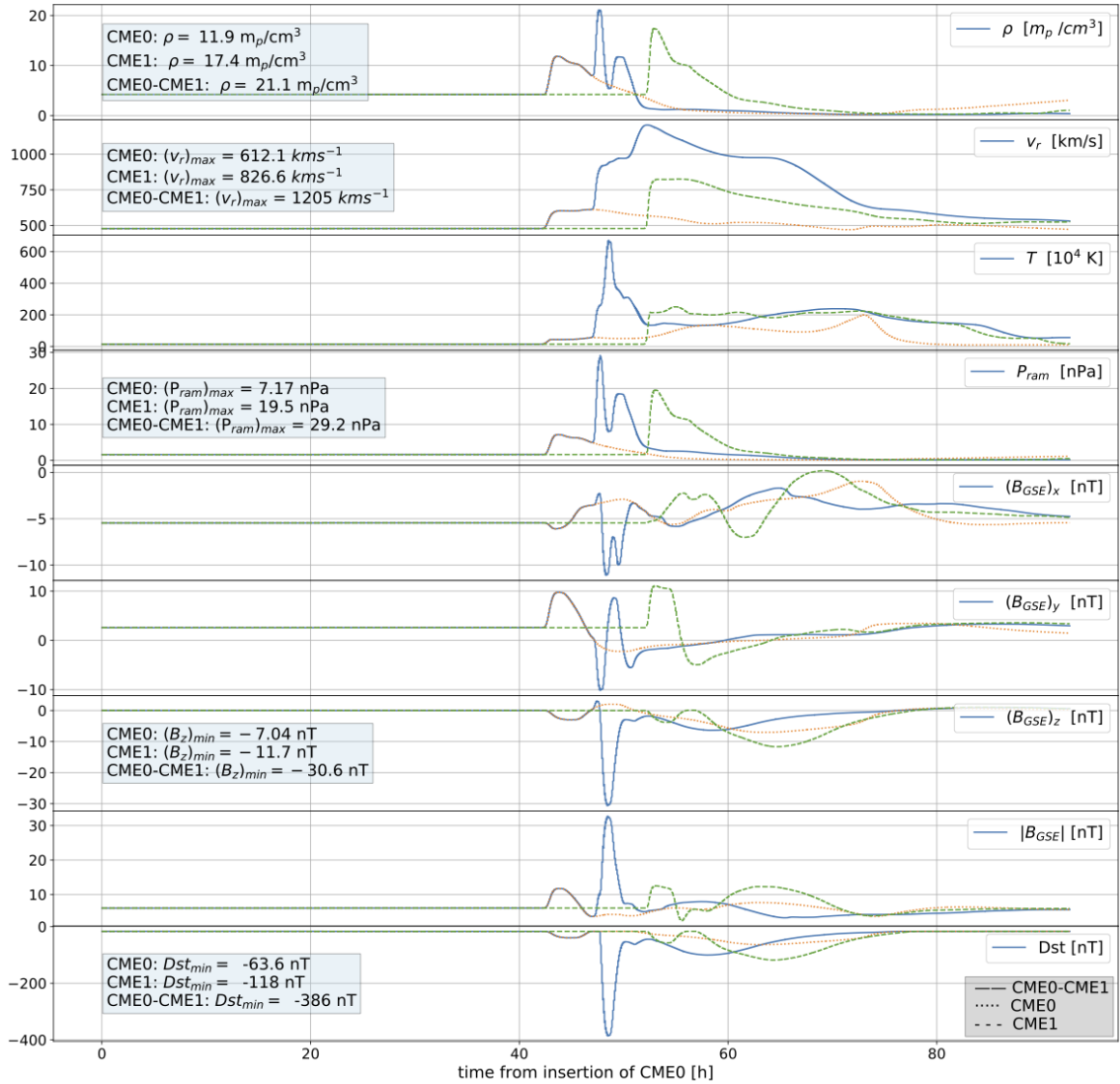


Figure 31: Virtual spacecraft data at 1 AU for a CME0-CME1 interaction of a waiting time of 24 h

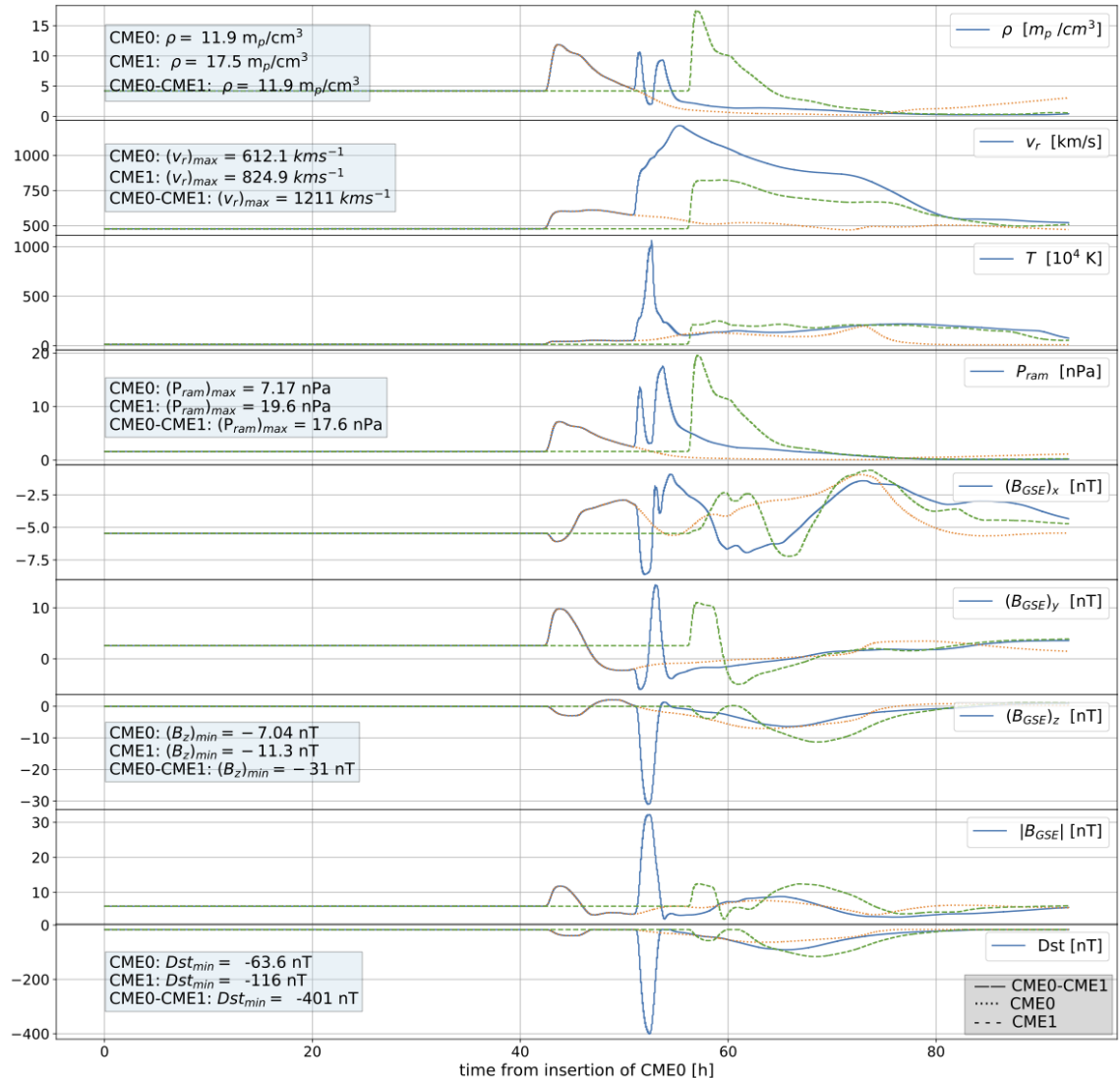


Figure 32: Virtual spacecraft data at 1 AU for a CME0-CME1 interaction of a waiting time of 28 h

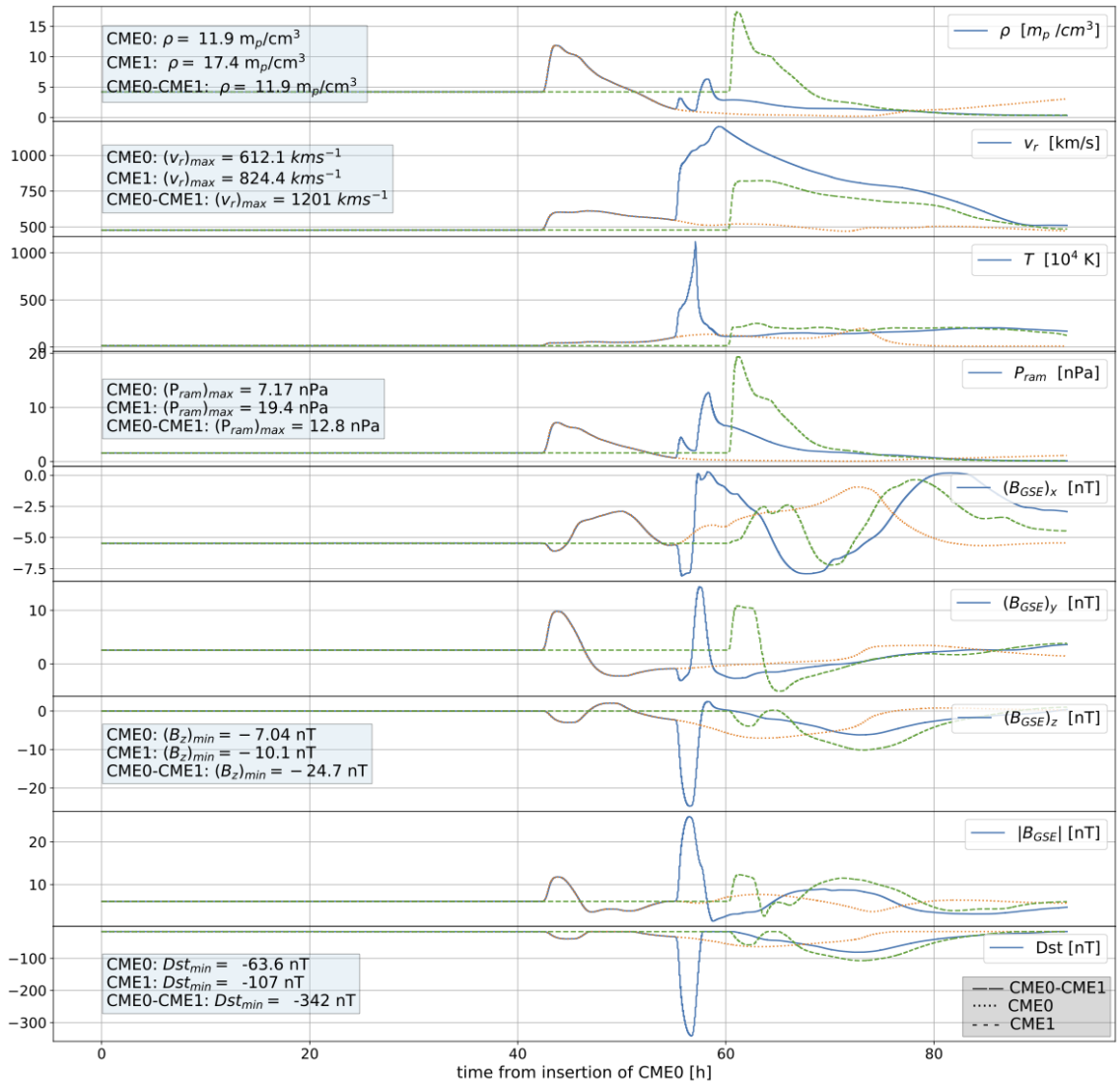


Figure 33: Virtual spacecraft data at 1 AU for a CME0-CME1 interaction of a waiting time of 32 h

Appendix F Handedness Simulation Runs

Here the remaining virtual spacecraft timeseries of Stage 3 are presented for completeness:

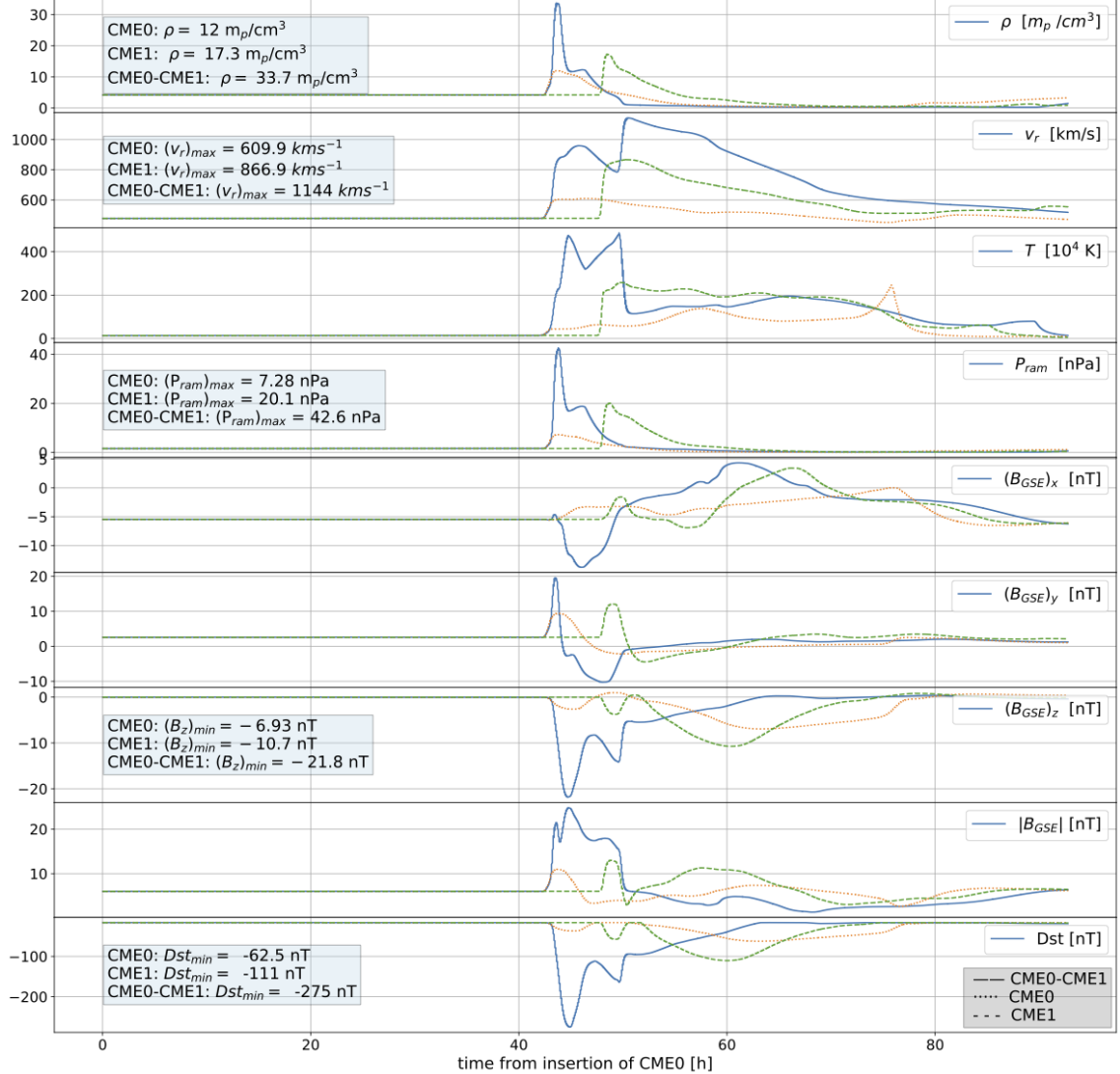


Figure 34: Virtual spacecraft timeseries at 1 AU for a CME0-CME1 interaction of Handedness $H_0 = 1$, $H_1 = 1$. (waiting time 20 h, both tilt angles $\tau = 180^\circ$)

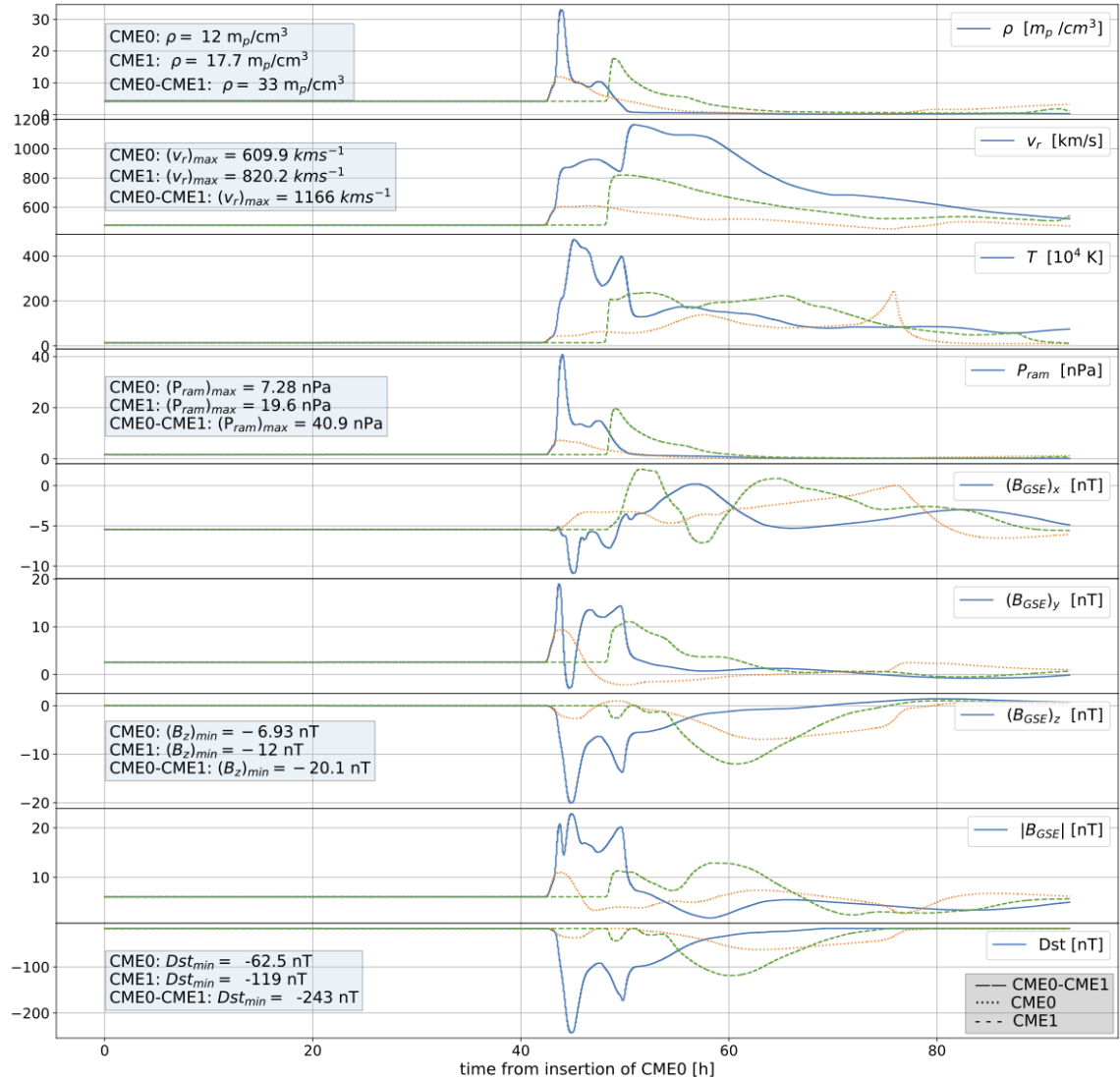


Figure 35: Virtual spacecraft timeseries at 1 AU for a CME0-CME1 interaction of Handedness $H_0 = 1$, $H_1 = -1$. (waiting time 20 h, both tilt angles $\tau = 180^\circ$)

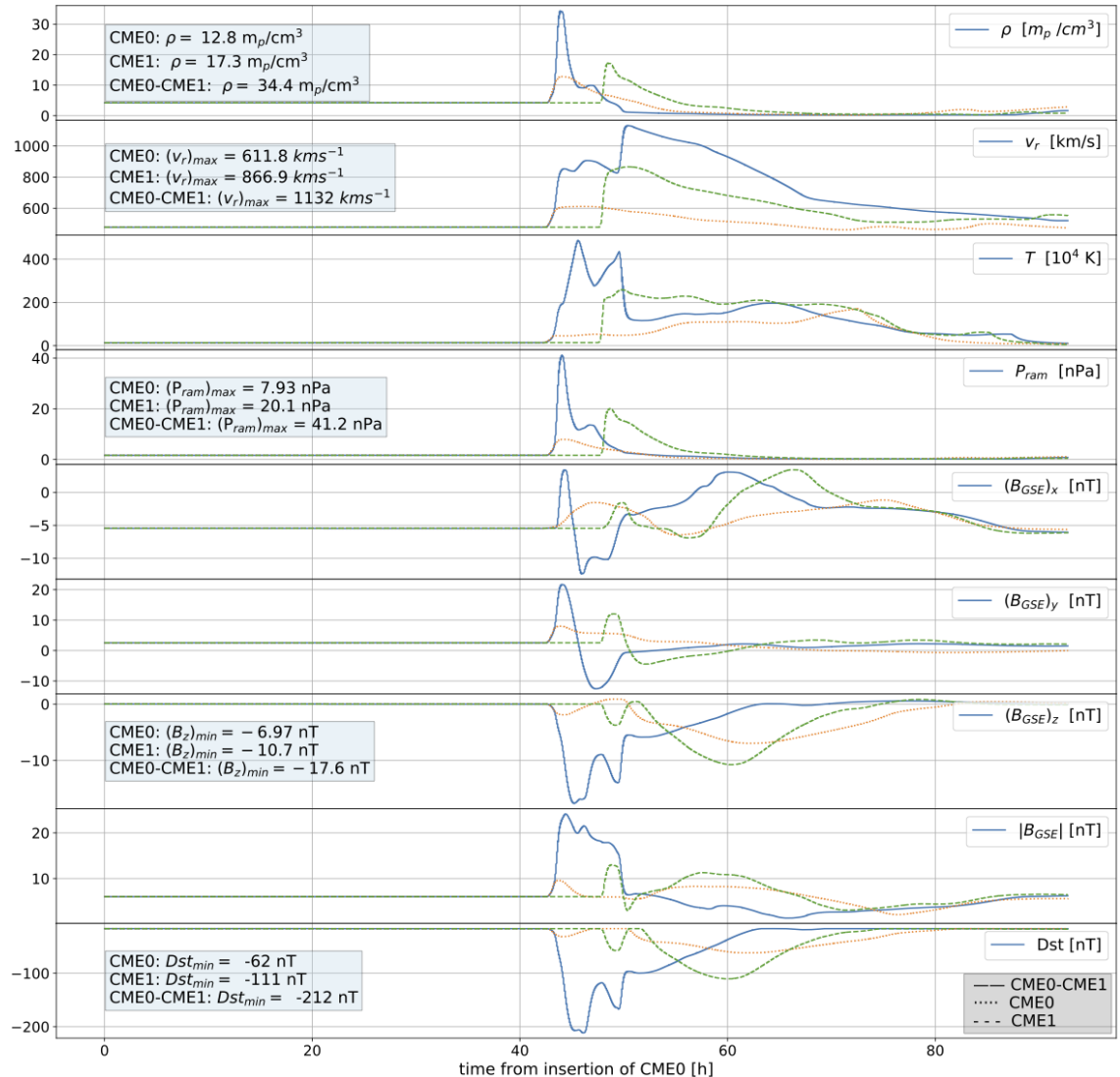


Figure 36: Virtual spacecraft timeseries at 1 AU for a CME0-CME1 interaction of Handedness $H_0 = -1$, $H_1 = 1$. (waiting time 20 h, both tilt angles $\tau = 180^\circ$)

References

- [1] P. J. Cargill, J. Chen, D. S. Spicer, and S. T. Zalesak. Magnetohydrodynamic simulations of the motion of magnetic flux tubes through a magnetized plasma. *Journal of Geophysical Research: Space Physics*, 101(A3):4855–4870, mar 1996.
- [2] J Zhang, I G Richardson, D F Webb, N Gopalswamy, E. Huterunen, J C Kasper, N V Nitta, W Poomvises, B J Thompson, C. C. Wu, S Yashiro, and A N Zhukov. Solar and interplanetary sources of major geomagnetic storms ($Dst \leq -100$ nT) during 1996-2005. *Journal of Geophysical Research: Space Physics*, 112(10):10102, 2007.
- [3] S. Vennerstrom, L. Lefevre, M. Dumbović, N. Crosby, O. Malandraki, I. Pat-sou, F. Clette, A. Veronig, B. Vršnak, K. Leer, and T. Moretto. Extreme Geomagnetic Storms - 1868 - 2010. *SoPh*, 291(5):1447–1481, may 2016.
- [4] Noé Lugaz, Manuela Temmer, Yuming Wang, and Charles J. Farrugia. The Interaction of Successive Coronal Mass Ejections: A Review. *Solar Physics*, 292(4), 2017.
- [5] Ying D Liu, Janet G Luhmann, Primož Kajdič, Emilia K.J. Kilpua, Noé Lugaz, Nariaki V Nitta, Christian Möstl, Benoit Lavraud, Stuart D Bale, Charles J Farrugia, and Antoinette B Galvin. Observations of an extreme storm in interplanetary space caused by successive coronal mass ejections. *Nature Communications*, 5(1):3481, may 2014.
- [6] Ravindra T Desai, Han Zhang, Emma E Davies, Julia E Stawarz, Joan Micco-Gomez, Pilar Iváñez-Ballesteros, and · Pilar Iváñez-Ballesteros. Three Dimensional Simulations of Solar Wind Preconditioning and the 23 July 2012 Interplanetary Coronal Mass Ejection. *Solar Physics*, 295(9):130, sep 2020.
- [7] Camilla Scolini, Emmanuel Chané, Manuela Temmer, Emilia K J Kilpua, Karin Dissauer, Astrid M Veronig, Erika Palmerio, Jens Pomoell, Mateja Dumbović, Jingnan Guo, Luciano Rodriguez, and Stefaan Poedts. CME-CME Interactions as Sources of CME Geoeffectiveness: The Formation of the Complex Ejecta and Intense Geomagnetic Storm in 2017 Early September. *The Astrophysical Journal Supplement Series*, 247:21, 2020.
- [8] Ming Xiong, Huinan Zheng, Yuming Wang, and Shui Wang. Magnetohydrodynamic simulation of the interaction between interplanetary strong shock and magnetic cloud and its consequent geoeffectiveness. *Journal of Geophysical Research: Space Physics*, 111(8):8105, 2006.
- [9] Hong Xie, Leon Ofman, and Gareth Lawrence. Cone model for halo CMEs: Application to space weather forecasting. *Journal of Geophysical Research: Space Physics*, 109(A3):1–13, 2004.
- [10] X. H. Xue, C. B. Wang, and X. K. Dou. An ice-cream cone model for coronal mass ejections. *Journal of Geophysical Research: Space Physics*, 110(A8):1–12, 2005.

- [11] D. Odstrčil and V. J. Pizzo. Three-dimensional propagation of coronal mass ejections (CMEs) in a structured solar wind flow: 2. CME launched adjacent to the streamer belt. *Journal of Geophysical Research: Space Physics*, 104(A1):493–503, 1999.
- [12] C. Verbeke, J. Pomoell, and S. Poedts. The evolution of coronal mass ejections in the inner heliosphere: Implementing the spheromak model with EUHFORIA. *Astronomy and Astrophysics*, 627:1–15, 2019.
- [13] C. Scolini, L. Rodriguez, M. Mierla, J. Pomoell, and S. Poedts. Observation-based modelling of magnetised coronal mass ejections with EUHFORIA. *Astronomy Astrophysics*, 626:A122, jun 2019.
- [14] Talwinder Singh, Tae K. Kim, Nikolai V. Pogorelov, and Charles N. Arge. Application of a Modified Spheromak Model to Simulations of Coronal Mass Ejection in the Inner Heliosphere. *Space Weather*, 18(5), 2020.
- [15] A. J. Hundhausen. Sizes and locations of coronal mass ejections: SMM observations from 1980 and 1984-1989. *Journal of Geophysical Research: Space Physics*, 98(A8):13177–13200, 1993.
- [16] A. J. Hundhausen, J. T. Burkepile, and O. C. St. Cyr. Speeds of coronal mass ejections: SMM observations from 1980 and 1984-1989. Technical Report A4, 1994.
- [17] S. E. Gibson and B. C. Low. A Time[U+2010]dependent Three[U+2010]dimensional Magnetohydrodynamic Model of the Coronal Mass Ejection. *The Astrophysical Journal*, 493(1):460–473, jan 1998.
- [18] Pete Riley. On the probability of occurrence of extreme space weather events. *Space Weather*, 10(2), 2012.
- [19] B. T. Tsurutani, W. D. Gonzalez, G. S. Lakhina, and S. Alex. The extreme magnetic storm of 1–2 September 1859. *Journal of Geophysical Research: Space Physics*, 108(A7), jul 2003.
- [20] C. T. Russell, R. A. Mewaldt, J. G. Luhmann, G. M. Mason, T. T. von Rosenvinge, C. M. S. Cohen, R. A. Leske, R. Gomez-Herrero, A. Klassen, A. B. Galvin, and K. D. C. Simunac. THE VERY UNUSUAL INTERPLANETARY CORONAL MASS EJECTION OF 2012 JULY 23: A BLAST WAVE MEDIATED BY SOLAR ENERGETIC PARTICLES. *The Astrophysical Journal*, 770(1):38, may 2013.
- [21] L. Van Driel-Gesztelyi and J. L. Culhane. Magnetic flux emergence, activity, eruptions and magnetic clouds: Following magnetic field from the sun to the heliosphere. *Space Science Reviews*, 144(1-4):351–381, 2009.
- [22] Thomas H Zurbuchen and Ian G Richardson. In-situ solar wind and magnetic field signatures of interplanetary coronal mass ejections. *Space Science Reviews*, 123(1-3):31–43, 2006.
- [23] G. Bodo, P. Rossi, A. Mignone, S. Massaglia, and A. Ferrari. Deceleration of relativistic jets. *New Astronomy Reviews*, 47(6-7):557–559, oct 2003.

- [24] A. Petralia, F. Reale, and P. Testa. Guided flows in coronal magnetic flux tubes. *Astronomy Astrophysics*, 609:A18, jan 2018.
- [25] J. D. Alvarado-Gómez, G. A. J. Hussain, O. Cohen, J. J. Drake, C. Garraffo, J. Grunhut, and T. I. Gombosi. Simulating the environment around planet-hosting stars - II. Stellar winds and inner astrospheres. *Astronomy Astrophysics*, 594:A95, oct 2016.
- [26] Pete Riley, Ronald M Caplan, Joe Giacalone, David Lario, and Ying Liu. PROPERTIES OF THE FAST FORWARD SHOCK DRIVEN BY THE 2012 JULY 23 EXTREME CORONAL MASS EJECTION. 2016.
- [27] A Mignone, G Bodo, S Massaglia, T Matsakos, O Tesileanu, C Zanni, and A Ferrari. PLUTO: A Numerical Code for Computational Astrophysics. *The Astrophysical Journal Supplement Series*, 170(1):228–242, 2007.
- [28] Julio David, Melon Fuksman, and Andrea Mignone. A Radiative Transfer Module for Relativistic Magnetohydrodynamics in the PLUTO Code. *The Astrophysical Journal Supplement Series*, 242:20, 2019.
- [29] E. N. Parker. Dynamics of the Interplanetary Gas and Magnetic Fields. *The Astrophysical Journal*, 128:664, nov 1958.
- [30] Barry T. Thomas, James A. Slavin, and Edward J. Smith. Radial and latitudinal gradients in the interplanetary magnetic field: Evidence for meridional flux transport. *Journal of Geophysical Research*, 91(A6):6760, jun 1986.
- [31] C Pei, J R Jokipii, and J Giacalone. Effect of a Random Magnetic Field on the Onset Times of Solar Particle Events. *The Astrophysical Journal*, 641(2):1222–1226, apr 2006.
- [32] T. L. Totten, J. W. Freeman, and S. Arya. An empirical determination of the polytropic index for the free-streaming solar wind using Helios 1 data. *Journal of Geophysical Research*, 100(A1):13, 1995.
- [33] Joshua E Stawarz, Charles W Smith, Bernard J Vasquez, Miriam A Forman, and Benjamin T. MacBride. The turbulent cascade and proton heating in the solar wind at 1 AU. *Astrophysical Journal*, 697(2):1119–1127, jun 2009.
- [34] M L Goldstein, R T Wicks, S Perri, and F Sahraoui. Kinetic scale turbulence and dissipation in the solar wind: Key observational results and future outlook, 2015.
- [35] Steven R Cranmer, William H Matthaeus, Benjamin A Breech, and Justin C Kasper. EMPIRICAL CONSTRAINTS ON PROTON AND ELECTRON HEATING IN THE FAST SOLAR WIND. *The Astrophysical Journal*, 702:1604–1614, 2009.
- [36] D. Odstrcil, P. Riley, and X. P. Zhao. Numerical simulation of the 12 May 1997 interplanetary CME event. *Journal of Geophysical Research: Space Physics*, 109(A2):1–8, 2004.

- [37] W. D. Gonzalez, J. A. Joselyn, Y. Kamide, H. W. Kroehl, G. Rostoker, B. T. Tsurutani, and V. M. Vasyliunas. What is a geomagnetic storm? *Journal of Geophysical Research*, 99(A4):5771, 1994.
- [38] D. Shiota and R. Kataoka. Magnetohydrodynamic simulation of interplanetary propagation of multiple coronal mass ejections with internal magnetic flux rope (SUSANOO-CME). *Space Weather*, 14(2):56–75, 2016.
- [39] David Shapakidze, Arnold Deboscher, Andria Rogava, and Stefaan Poedts. Consistent self-similar magnetohydrodynamics evolution of coronal transients. *Astrophysical Journal*, 712(1):565–573, 2010.
- [40] V. S. Titov, T. Török, Z. Mikic, and J. A. Linker. A method for embedding circular force-free flux ropes in potential magnetic fields. *Astrophysical Journal*, 790(2), 2014.
- [41] R. Kataoka, T. Ebisuzaki, K. Kusano, D. Shiota, S. Inoue, T. T. Yamamoto, and M. Tokumaru. Three-dimensional MHD modeling of the solar wind structures associated with 13 December 2006 coronal mass ejection. *Journal of Geophysical Research: Space Physics*, 114(10):1–10, 2009.
- [42] M. Janvier, P. Démoulin, and S. Dasso. Global axis shape of magnetic clouds deduced from the distribution of their local axis orientation. *Astronomy Astrophysics, Volume 556, id.A50, <NUMPAGES>13</NUMPAGES> pp.*, 556:A50, aug 2013.
- [43] Yuming Wang, Chenglong Shen, Rui Liu, Jiajia Liu, Jingnan Guo, Xiaolei Li, Mengjiao Xu, Qiang Hu, and Tielong Zhang. Understanding the Twist Distribution Inside Magnetic Flux Ropes by Anatomizing an Interplanetary Magnetic Cloud. *Journal of Geophysical Research: Space Physics*, 123(5):3238–3261, may 2018.
- [44] S Chandrasekhar. ON FORCE-FREE MAGNETIC FIELDS. Technical report, 1956.
- [45] Maxim Lyutikov and Konstantinos Nektarios Gourgouliatos. MAGNETIC STRUCTURE OF CORONAL MASS EJECTIONS.
- [46] Dinshaw S. Balsara and Daniel Spicer. Maintaining Pressure Positivity in Magnetohydrodynamic Simulations. *Journal of Computational Physics*, 148(1):133–148, jan 1999.
- [47] A Mignone, B Vaidya, D Mukherjee, G Mattia, J D Melon Fuksman, O Tesileanu, and T Matsakos. PLUTO - User ' s Guide Terms Conditions of Use. 4(405), 2020.
- [48] Jens Pomoell and S. Poedts. EUHFORIA: European heliospheric forecasting information asset. *Journal of Space Weather and Space Climate*, 8:A35, 2018.
- [49] Nikolai Pogorelov, Sergey Borovikov, Jacob Heerikhuisen, Tae Kim, Igor Kryukov, and Gary Zank. MS-FLUKSS and its application to modeling flows of partially ionized plasma in the heliosphere. In *ACM International Conference Proceeding Series*. Association for Computing Machinery, 2014.

- [50] NOAA. NOAA Space Weather Scales | NOAA / NWS Space Weather Prediction Center.
- [51] C.-C. Wu and R.P. Lepping. Relationships for predicting magnetic cloud-related geomagnetic storm intensity. *Journal of Atmospheric and Solar-Terrestrial Physics*, 67(3):283–291, feb 2005.
- [52] L. Burlaga, E. Sittler, F. Mariani, and R. Schwenn. Magnetic loop behind an interplanetary shock: Voyager, Helios, and IMP 8 observations. *Journal of Geophysical Research*, 86(A8):6673, aug 1981.
- [53] G. L. Siscoe and R. W. Suey. Significance criteria for variance matrix applications. *Journal of Geophysical Research*, 77(7):1321–1322, mar 1972.